J. Fluid Mech. (1989), *vol.* 200, *pp.* 563–594
Printed in Great Britain

Direct numerical simulation of stratified homogeneous turbulent shear flows

By T. GERZ,† U. SCHUMANN† AND S. E. ELGHOBASHI‡

†DLR, Institute of Atmospheric Physics, D-8031 Oberpfaffenhofen, Federal Republic of Germany

‡Department of Mechanical Engineering, University of California, Irvine, CA 92717, USA

(Received 15 March 1988)

The exact time-dependent three-dimensional Navier–Stokes and temperature equations are integrated numerically to simulate stably stratified homogeneous turbulent shear flows at moderate Reynolds numbers whose horizontal mean velocity and mean temperature have uniform vertical gradients. The method uses shear-periodic boundary conditions and a combination of finite-difference and pseudospectral approximations. The gradient Richardson number Ri is varied between 0 and 1. The simulations start from isotropic Gaussian fields for velocity and temperature both having the same variances.

The simulations represent approximately the conditions of the experiment by Komori *et al.* (1983) who studied stably stratified flows in a water channel (molecular Prandtl number $Pr = 5$). In these flows internal gravity waves build up, superposed by hot cells leading to a persistent counter-gradient heat-flux (CGHF) in the vertical direction, i.e. heat is transported from lower-temperature to higher-temperature regions. Further, simulations with $Pr = 0.7$ for air have been carried out in order to investigate the influence of the molecular Prandtl number. In these cases, no persistent CGHF occurred. This confirms our general conclusion that the counter-gradient heat flux develops for strongly stable flows ($Ri \approx 0.5$–1.0) at sufficiently large Prandtl numbers ($Pr = 5$). The flux is carried by hot ascending, as well as cold descending turbulent cells which form at places where the highest positive and negative temperature fluctuations initially existed. Buoyancy forces suppress vertical motions so that the cells degenerate to two-dimensional fossil turbulence. The counter-gradient heat flux acts to enforce a quasi-static equilibrium between potential and kinetic energy.

Previously derived turbulence closure models for the pressure–strain and pressure–temperature gradients in the equations for the Reynolds stress and turbulent heat flux are tested for moderate-Reynolds-number flows with strongly stable stratification ($Ri = 1$). These models overestimate the turbulent interactions and underestimate the buoyancy contributions. The dissipative timescale ratio for stably stratified turbulence is a strong function of the Richardson number and is inversely proportional to the molecular Prandtl number of the fluid.

1. Introduction

The objective of this study is to investigate the effects of stable stratification and shear on the behaviour and the evolution of homogeneous turbulent flows using the method of direct numerical simulation. A numerical method has been developed to integrate the exact time-dependent three-dimensional Navier–Stokes and

temperature equations in a cubic domain and in time. Owing to the limited storage capacity of current computers, the simulation is restricted to moderate Reynolds numbers.

The study is motivated by the need to understand and predict the structure of stratified turbulent shear flows which occur in practical and atmospheric flows. However, this work considers only homogeneous turbulence in which the mean velocity and temperature have a uniform gradient in the vertical direction. In homogeneous turbulence, spatial gradients of turbulent correlations vanish in the statistical mean (Batchelor 1953) so that the divergence of diffusive fluxes is zero. This fact simplifies the analysis and allows one to study the effects of shear and stratification without the complication of diffusion. Shear intensifies the turbulent fluctuations, whereas the temperature gradient generally attenuates them by converting kinetic energy into 'available potential energy' (Gill 1982). The available potential energy is proportional to the mean square of density fluctuations or temperature fluctuations in the Boussinesq approximation. It measures the amount of kinetic energy that is created by gravity forces if the fluid undergoes vertical motions which bring each fluid element to a level where the local density equals the mean density. The combined effects of shear and buoyancy forces produce anisotropic and scale-dependent structures.

Stillinger, Helland & Van Atta (1983) and Itsweire, Helland & Van Atta (1986) carried out experiments in stably stratified, unsheared salt-water flows with turbulent density fluctuations. As the flow developed, buoyancy forces became increasingly dominant, produced internal gravity waves and reduced the fluctuations to two-dimensional 'fossil' turbulence (Gibson 1987). The direct simulations of Riley, Metcalfe & Weissman (1981) provided similar results in spite of the rather small Reynolds number used in the simulations.

Homogeneous turbulent shear flows with temperature gradients imposed in the same direction as that of mean velocity have been studied in a wind tunnel by Tavoularis & Corrsin (1981) and Budwig, Tavoularis & Corrsin (1985). The temperature variations were passive (small Richardson number) and behaved like the velocity fluctuations, i.e. variance and integral lengthscales increased monotonically and the correlation coefficient of the vertical heat flux reached a value of -0.45. The correlation coefficient of the vertical momentum flux in neutrally stratified shear flows reaches about the same value (Champagne, Harris & Corrsin 1970; Harris, Graham & Corrsin 1977). Direct numerical simulations of this type of flow has been performed by Rogallo (1981) and Shirani, Ferziger & Reynolds (1981) as summarized in Rogallo & Moin (1984), and by Baron (1982), Laurence (1986), and Rogers & Moin (1987). Shirani *et al.* (1981) studied the mixing behaviour of a passive scalar in isotropic decaying turbulence as well as in homogeneous shear turbulence with a mean temperature gradient. Rogers, Moin & Reynolds (1986) superposed temperature gradients in directions perpendicular to the shear direction also. They were interested in the transport of the passive scalar and its dependence on the coherent vortex structures of the shear flow. Gerz (1988*b*) studied the influence of different stable stratifications on such coherent structures in shear flows.

Komori *et al.* (1983) measured velocity and temperature fluctuations in a stably stratified shear flow in a water channel. They measured in the fully developed flow region a mean vertical heat flux in the direction of increasing mean temperature, the so-called counter-gradient heat flux (CGHF), accompanied by a change of flow from a fully turbulent state to one dominated by a gravity wave field. Komori *et al.* associated these positive heat fluxes with hot ascending eddies superimposed on the

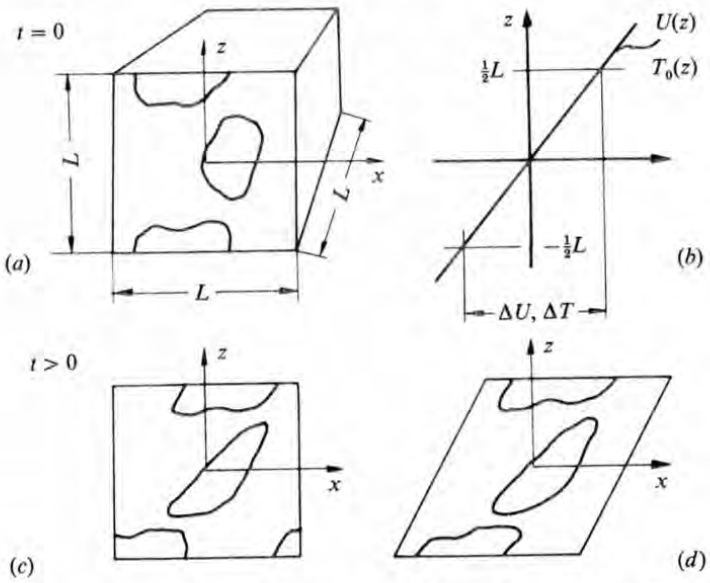

FIGURE 1. Sketch of the computational domain and the mean profiles. (*a*) The cubical flow domain; (*b*) mean velocity and temperature profiles $U(z), T_0(z)$; (*c*) flow field in Eulerian frame of reference after some time; (*d*) same flow field in a Lagrangian frame. In this paper, the Eulerian frame is being used.

waves. Webster (1964) investigated stratified homogeneous shear flows in a wind tunnel, and did not find a CGHF. One purpose of this paper is to explain this difference.

Second-order turbulence closure models as proposed by Launder (1975, 1976) for stably stratified shear flows are of great utility for prediction of geophysical or engineering flows but contain model coefficients which in most cases require empirical adjustment. Our ultimate goal is to use the results of our simulations of stratified shear flows to calibrate existing second-order turbulence closure models. As a first step, we test the models of the pressure–strain and the pressure–temperature gradient correlations which – besides dissipation – are the most important terms in second-order closure models for the flows considered here. Further, an estimate of the dissipative timescale ratio for velocity and temperature will be given for flows with highly stable stratification where the influence of the shear forces is negligible. This timescale ratio is needed to validate closure models of the pressure–temperature correlation and the thermal dissipation rate (Warhaft & Lumley 1978; Elghobashi & Launder 1983).

The domain and the mean profiles for velocity and temperature are illustrated in figure 1 (*a*, *b*). Shear imposes a problem with respect to the boundary conditions. The common choice of boundary conditions in direct numerical simulations of homogeneous turbulence is periodicity in all spatial directions. However, in the presence of shear, a field which is initially periodic in the vertical direction soon becomes non-periodic. For illustration, we assume that two parcels of fluid located above each other have the same properties initially. As time proceeds, the parcels are displaced relative to each other in the horizontal direction owing to different horizontal velocities. Thus the common periodicity condition cannot be used in the vertical direction. Rogallo (1981) solved this problem by using a time-dependent coordinate transformation which corresponds to a Lagrangian reference frame, as

illustrated in figure 1(*d*). In this frame of reference, the flow may be assumed to be periodic in the direction of the transformed coordinate. This makes it possible to apply Fourier-spectral approximations of the fields with respect to this coordinate. This method has been used for several studies by the Stanford group, e.g. see Rogers & Moin (1987). The disadvantage of this approach is the need for remeshing at a frequency $\frac{1}{2}\mathrm{d}U/\mathrm{d}z$, which causes interpolation errors of the aliasing type (Shirani *et al.* 1981). This approach has not yet been applied to cases with buoyancy forces and it is not clear what difficulties might arise in this method because of the time-dependence of the components of the gravity vector in the transformed coordinates. Here, we use the alternative approach, originally proposed for pure shear flows by Baron (1982), where the equations are discretized in the Eulerian reference frame sketched in figure 1(*c*) using the so-called 'shear-periodic' boundary condition (Schumann 1985). This condition, stated precisely in equation (4), assumes periodicity in a direction that varies as a function of time. It corresponds to continuous remapping by applying horizontal periodicity and avoids interruptions at discrete times. This type of boundary condition is not applicable to Fourier-spectral approximations in the vertical but can easily be implemented in a finite-difference scheme.

The details of the mathematical approach and numerical procedure are described in §2. The results of the numerical simulations for various Richardson and Prandtl numbers will be discussed and compared with the experimental data of Komori *et al.* (1983) and Webster (1964) in §3. Special attention is given in §4 to the analysis of the counter-gradient heat flux. Parameters of second-order turbulence closure models and the dissipative timescale ratio will be investigated in §5. Section 6 summarizes the results.

2. Mathematical description

2.1. *Computational domain and equations*

We consider a finite cubical domain with side length L. The mean horizontal velocity $U(z)$ and mean temperature $T_0(z)$ possess uniform and constant gradients relative to the vertical coordinate z. The fluid is assumed to have constant diffusivities ν and γ for momentum and heat, respectively. The Boussinesq approximation is used, i.e. we assume that the density ρ_0 is constant except for small density fluctuations due to temperature fluctuations affecting buoyancy accelerations. Subsequently all fields are expressed non-dimensionally using ρ_0, L, $\Delta U = |\mathrm{d}U/\mathrm{d}z|\,L$, and $\Delta T = |\mathrm{d}T_0/\mathrm{d}z|L$ as reference scales for density, length, velocity, and temperature, respectively.

The normalized Navier–Stokes equation, the heat balance and the continuity equation read respectively

$$\frac{\partial u_i}{\partial t}+\frac{\partial}{\partial x_j}(u_j u_i)+Sx_3\frac{\partial u_i}{\partial x_1}+Su_3\delta_{i1}=\frac{1}{Re}\frac{\partial^2 u_i}{\partial x_j^2}-\frac{\partial p}{\partial x_i}+|Ri|T\delta_{i3},\quad i=1,2,3, \tag{1}$$

$$\frac{\partial T}{\partial t}+\frac{\partial}{\partial x_j}(u_j T)+Sx_3\frac{\partial T}{\partial x_1}+su_3=\frac{1}{Re\,Pr}\frac{\partial^2 T}{\partial x_j^2}, \tag{2}$$

$$\frac{\partial u_j}{\partial x_j}=0, \tag{3}$$

where the summation convention is used and u_i, T and p are the deviations of the instantaneous velocity, temperature and pressure from their respective mean profiles. The non-dimensional shear $S = (L/\Delta U)\,(\mathrm{d}U/\mathrm{d}z) = 0,\ 1$ and stratification $s = (L/\Delta T)\,(\mathrm{d}T_0/\mathrm{d}z) = -1,\ 0,\ 1$ are introduced as parameters in order to distinguish between cases with and without shear and with unstable, neutral and stable stratification, respectively. Terms in the above equations containing S or s describe advection due to the mean profiles. The Reynolds number $Re = \Delta U L/\nu$, the absolute value of the Richardson number $Ri = s\alpha g\, L\Delta T/(\Delta U)^2$ and the Prandtl number $Pr = \nu/\gamma$ are the independent parameters characterizing the flow where α and g are the constant isobaric volumetric expansion coefficient and the gravitational acceleration. The values of the dimensionless spatial coordinates x_i are within the range $-\frac{1}{2} \leqslant x_i \leqslant \frac{1}{2}$, and x_3 points vertically upwards. The boundary conditions for any fluctuation $f \in \{u_1, u_2, u_3, T, p\}$ read

$$f(t, x_1 + m_1, x_2 + m_2, x_3 + m_3) = f(t, x_1 - S m_3 t, x_2, x_3), \tag{4}$$

where m_i are arbitrary integers.

The equations are discretized in an Eulerian framework using a second-order finite-difference technique on a staggered grid for all the terms in the equations except the mean advection where pseudospectral (Fourier) approximation is used. The Adams–Bashforth scheme is used to integrate the equations in time. Pressure is treated implicitly. The acceleration terms, which are treated explicitly by finite differences, are

$$r_i = \frac{1}{Re}\delta_j \delta_j u_i + |Ri|\overline{T}^3\,\delta_{i3} - \delta_j(\overline{u}_j^i\,\overline{u}_i^j) - S\overline{u}_3^{1\,-3}\,\delta_{i1}, \tag{5}$$

where $\delta_j f$ denotes the common central finite-difference operator and $\overline{f}^j$ the algebraic average of two discrete neighbouring grid values f separated by one grid interval in direction of the coordinate x_j. The integration of velocity from time level n to $n+1$ proceeds in three steps. We start from

$$u_i^* = u_i^n + \Delta t[w_1 r_i^n - w_2 r_i^{n-1}], \tag{6}$$

with weights $w_1 = 1$, $w_2 = 0$ for $n = 0$; $w_1 = \frac{3}{2}$, $w_2 = \frac{1}{2}$ for $n > 0$. Then we obtain the next refinement of the velocity $\tilde{u}_i$ at x_1 by evaluating u_i^* at the upstream position from where it is advected by the mean velocity Sx_3 during the time-step Δt, using discrete Fourier interpolation,

$$\tilde{u}_i(x_1) = u_i^*(x_1 - \Delta t\, S x_3). \tag{7}$$

The boundary conditions are applied to these velocities so that the divergence can be determined in the next step. The pressure p^{n+1} at the new time level is obtained by solving the Poisson equation in finite-difference form

$$\delta_i \delta_i p^{n+1} = \frac{1}{\Delta t}\delta_i \tilde{u}_i. \tag{8}$$

The solution of (8) is obtained using a fast Poisson solver (Schumann 1985) which includes the shear-periodic boundary condition at time t^{n+1} and applies a combination of fast Fourier transforms and Gaussian elimination. Imposing the pressure boundary conditions at time t^{n+1}, i.e. using the same time level as in (7) when calculating $\tilde{u}_i$, is essential in this algorithm to get correct results. Finally we obtain the solution

$$u_i^{n+1} = \tilde{u}_i - \Delta t\,\delta_i p^{n+1}, \tag{9}$$

which satisfies the continuity equation. Temperature is integrated likewise with $T^{n+1} \equiv \tilde{T}$. Now, the fields are adjusted to the remaining boundary conditions by applying (4) at time level $n+1$. The boundary condition (4) requires interpolation in x_1 unless the time step Δt equals the grid spacing Δx. Baron (1982) applied this method for $\Delta t = \Delta x$. From a linear analysis, we found it necessary for numerical stability to reduce the time step to a fraction of the grid spacing. In the present case we use $\Delta t = \Delta x/2$. Therefore, (4) is evaluated by means of Fourier interpolation. Further details of the numerical techniques are described in Schumann, Elghobashi & Gerz (1986) and in Gerz (1988*a*), where several validation tests are also reported. Tests for isotropic turbulence have shown that the energy decay rate and the velocity skewness are computed to the same accuracy of a spectral method but the spectral method requires only about half the resolution. Evaluation of mean advection by Fourier interpolation gives results which satisfy the condition of invariance under Galilean transformation. It is difficult to achieve this invariance with pure finite-difference schemes (Laurence 1986). Moreover, the results are homogeneous in the vertical direction in spite of the explicit appearance of the coordinate value x_3 in the equations.

2.2. *Initialization parameters*

The initial fluctuation fields of velocity and temperature are generated from Gaussian random numbers with defined spectra for the variances (Schumann 1985). The initialized fields are periodic in the three spatial directions and the velocity is divergence-free with respect to the discretized form of the continuity equation.

The initialization parameters are selected to simulate the water channel experiment of Komori *et al.* (1983) for a stably stratified, homogeneous turbulent shear flow. In that experiment the shear is due to the friction of the mean flow at the boundary layer along the bottom of the channel and the stratification is due to heating at the water surface by means of condensing steam. The stratified layer between $0.4 < z/\delta < 0.75$ (δ is the flow depth and z the height above channel bottom) was presumed by the experimentalists to be free of wall effects and a good approximation to a homogeneous shear flow. Our simulation results will corroborate this presumption. In the experiment, turbulence measurements for a wide range of values of the local gradient Richardson number ($Ri = 0$ to 1) were obtained. The Taylor microscale is unknown so that we cannot deduce a value of the turbulence Reynolds number but the 'channel Reynolds number' related to the hydraulic radius of the channel and the cross-sectional mean velocity varied from 9100 to 17000, which is rather small. Nothing is reported about the values of the initial turbulence correlations or energy spectra. Therefore, the initial isotropic turbulence in the simulation has been assumed to have the parameters and the spectrum reported in table 1.

The number of grid points is 64 in all three directions. This value is about the maximum one can achieve on a CRAY-1 computer because of limited storage capacities. Besides the Richardson and Prandtl numbers, independent input parameters are the peak wavenumber of the initial spectrum k_p, the root-mean-squares (r.m.s.) velocity v, the turbulence Reynolds number based on the Taylor microscale and the r.m.s. velocity, and the temperature variance $\overline{T'T'}$. All other quantities are derived from these values. The peak integer wavenumber is selected to be large enough that the integral lengthscale may grow during the simulation period. Also, it is selected to be large enough to obtain an adequate number of independent data points in the numerical scheme at wavenumbers below this peak

Physical parameters		
Peak integer wavenumber	k_p	6
Root-mean-square velocity	$v = (\overline{u_i u_i}/3)^{\frac{1}{2}}$	0.01644
Root-mean-square temperature	$T' = (\overline{TT})^{\frac{1}{2}}$	0.01644
Turbulence Reynolds number	$Re_\lambda = v\lambda/\nu$	24.7
Molecular Prandtl number	$Pr = \nu/\gamma$	0.7, 5
Gradient Richardson number	$Ri = s\alpha g L\Delta T/(\Delta U)^2$	0, 0.1, 0.2, 0.3, 0.5, 1
Three-dimensional initial energy spectrum	$\hat{E}(k) = \frac{1}{2\pi}\frac{3v^2}{2}\frac{k}{k_p^2}e^{-k/k_p}$	
Turbulence kinetic energy	$E = \frac{3}{2}v^2 = \frac{1}{2}\overline{u_i u_i}$	4.054×10^{-4}
Energy dissipation rate	$\epsilon = 8\pi^2 Re^{-1}\int k^2\hat{E}(k)\,dk = \frac{1}{2}\epsilon_{ii}$	1.042×10^{-4}
Reynolds stresses	$\overline{u_i u_j}$	2.703×10^{-4}, $i = j$ 0, $i \neq j$
Heat fluxes	$\overline{u_i T}$	0
Dissipation rates of the Reynolds stresses	$\epsilon_{ij} = \frac{2}{Re}\overline{\frac{\partial u_i}{\partial x_k}\frac{\partial u_j}{\partial x_k}}$	0.695×10^{-4}, $i = j$ 0, $i \neq j$
Dissipation rate of the temperature variance	$\epsilon_{TT} = \frac{2}{Re\,Pr}\overline{\frac{\partial T}{\partial x_k}\frac{\partial T}{\partial x_k}}$	0.992×10^{-4}, $Pr = 0.7$ 0.139×10^{-4}, $Pr = 5$
Dissipation rates of the heat fluxes	$\epsilon_{iT} = \frac{1+Pr}{Re\,Pr}\overline{\frac{\partial T}{\partial x_k}\frac{\partial u_i}{\partial x_k}}$	0
Pressure–strain correlation	$\phi_{ij} = \overline{p\left(\frac{\partial u_i}{\partial x_j}+\frac{\partial u_j}{\partial x_i}\right)}$	0
Pressure–temperature correlation	$\phi_{iT} = \overline{p\frac{\partial T}{\partial x_i}}$	0
Integral lengthscale	$l = (2v)^{-2}\int k^{-1}\hat{E}(k)\,dk$	0.0495
Taylor microscale	$\lambda = (15v^2(Re\,\epsilon)^{-1})^{\frac{1}{2}}$	0.0259
Kolmogorov lengthscale	$\eta = (Re^3\epsilon)^{-\frac{1}{4}}$	0.0026
Reynolds numbers	$Re = \Delta UL/\nu$, $Re_l = vl\,Re$	58060, 47.2
Shear number	$Sh = Sl/v$	3.01

Numerical parameters					Comparison with experiment at	
					time	step
M	Δx	Δt	t_{max}	time steps		
64	$1/M$	$\Delta x/2$	6.0	768	4.5	576

TABLE 1. Definitions and values of the dimensionless initialization parameters. The overbar denotes the spatial averaging operator (sum over all grid points)

wavenumber. For a smaller peak wavenumber, the statistics of large-scale components would be poorer. On the other hand, the peak wavenumber has to be small enough that the energy, the viscous dissipation and especially the thermal dissipation rates are sufficiently small at the largest resolved wavenumber $k_{max} = 32$. Figure 2 shows that this requirement is adequately met for viscous dissipation when

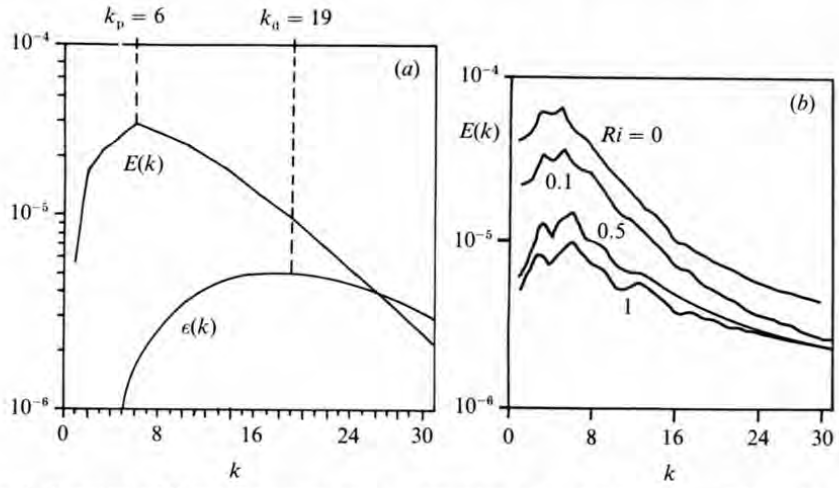

FIGURE 2. Spectra of kinetic energy and dissipation rate. (*a*) Spectra of E and ϵ at $t = 0$; (*b*) spectra of E at $t = 6$ for $Ri = 0$, 0.1, 0.5 and 1.

using the parameters selected here. Corresponding spectra of temperature variance show smooth and decaying behaviour at early times. At later times ($t > 3$), some variance piles up near the upper wavenumber limit but we have no indication that these limitations are important. The energy spectrum determines the values of the integral lengthscale l. The r.m.s. velocity v is chosen to give a suitable value of the shear number Sh. For too small a shear number, the integration time would have to be very large to obtain a quasi-steady state, as discussed by Harris *et al.* (1977). For too large a shear number, the nonlinear turbulent–turbulent interactions are small in comparison to mean-shear turbulence interactions. From preliminary parameter studies the value $Sh \approx 3$ has been found to be optimal in this sense. This value is close to those in wind tunnels as summarized by Rogers & Moin (1987), which typically vary between $Sh = 2.0$ (Champagne *et al.* 1970) and 2.8 (Tavoularis & Corrsin 1981). The Reynolds number Re_λ is taken such that the spectra near the cut-off wavenumber $k_{\max} = 32$ stay small enough for accurate simulations. The selected value and the resolutions are the same as used by Riley, Metcalfe & Weissman (1981). It is however smaller by a factor of about ten than the values used in wind-tunnel experiments, see the summary in Rogers & Moin (1987). Despite this, the resultant large-scale Reynolds number $Re = \Delta UL/\nu$ is quite large and even larger than the channel Reynolds number reported by Komori *et al.* (1983). The Kolmogorov scale is considerably smaller than the grid spacing but the grid-shear Reynolds number introduced by Rogers & Moin (1987) is of reasonable magnitude, $\Delta x(SRe)^{\frac{1}{2}} = 3.8$, and even a little less than the value used by Rogers & Moin. The initial temperature variance is set to $\overline{TT} = v^2$, which is a rather arbitrary selection but it ensures that temperature and velocity fluctuations have the same order of magnitude. In order to consider the influence of the initial conditions on the developing flow, we also performed a calculation with zero temperature variance initially and $Ri = 1$. In agreement with calculations using the rapid distortion theory (Hunt, Stretch & Britter 1988), we found that the oscillation amplitudes of $\overline{ww}$ and $\overline{wT}$ are larger for $\overline{TT} = 0$ initially. However, in both cases ($\overline{TT}_0 = v_0^2$ and $\overline{TT}_0 = 0$) a persistent positive vertical heat flux was established in the flow, as will be discussed below.

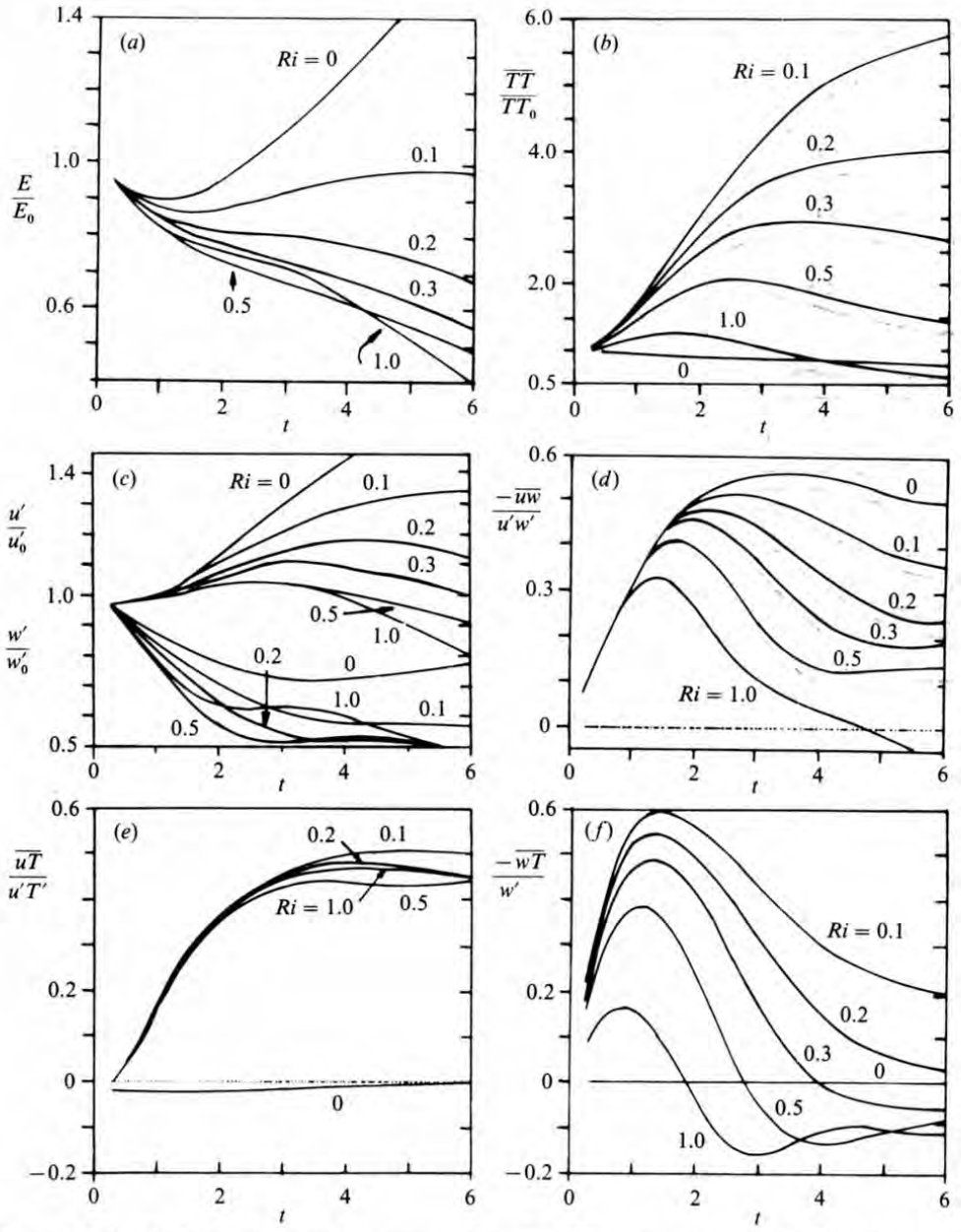

FIGURE 3. Turbulence mean values versus time for different values of the Richardson number Ri as obtained from the simulations. (*a*) Kinetic energy, (*b*) temperature variance, (*c*) r.m.s. values of u (upper curves) and w (lower curves); the correlation coefficients of (*d*) the negative vertical momentum flux, (*e*) the downstram heat flux and (*f*) the negative vertical heat flux. The quantities in (*a*), (*b*) and (*c*) are normalized by their initial values. In (*c*) (w'/w'_0) and (*e*) the data for $Ri = 0.3$ are omitted for clarity because they do not give any additional information.

3. Results and discussion

3.1. *Time development of the turbulence statistics*

Mean qualities are obtained by ensemble averaging of all their point values in the computational domain at a given time. Figure 3 depicts the dynamic development of various mean quantities for different values of the gradient Richardson number.

The results are normalized either by the initial values (subscript 0) or by the actual r.m.s. values. In the absence of buoyancy, we see that the turbulence energy increases owing to its production by the work of the shear against the developing vertical momentum flux, as expected. With increasing Richardson number, stable stratification damps the turbulent motion. When the Richardson number exceeds a critical value, the damping due to buoyancy balances the energy production rate due to shear. Figure 3(a) suggests a critical gradient Richardson number of about 0.1 which is smaller than the value of 0.25 for the linear case (Miles 1961). However, for very strong stability ($Ri = 1$), energy decreases at a slower rate, see figure 3(*a*). Also the r.m.s. value of the vertical velocity component w', which one would expect to decrease monotonically with increasing stability (Webster 1964; Launder 1975), shows a similar behaviour to the energy for the largest Richardson number, see figure 3(*c*).

In order to understand this change in the trend of E and its components one has to examine the dynamic behaviour of the fluxes and their interactions using the corresponding balance equations. After spatial averaging in the periodic domain for homogeneous turbulence, the dimensionless equations of the non-zero components of the Reynolds stresses, the kinetic energy, the heat fluxes and the temperature variance read respectively (see table 1 for the nomenclature):

$$\frac{\mathrm{d}\overline{uu}}{\mathrm{d}t} = -2S\,\overline{uw} + \phi_{11} - \epsilon_{11}, \tag{10}$$

$$\frac{\mathrm{d}\overline{vv}}{\mathrm{d}t} = \phi_{22} - \epsilon_{22}, \tag{11}$$

$$\frac{\mathrm{d}\overline{ww}}{\mathrm{d}t} = 2|Ri|\,\overline{wT} + \phi_{33} - \epsilon_{33}, \tag{12}$$

$$\frac{\mathrm{d}\overline{uw}}{\mathrm{d}t} = -S\,\overline{ww} + |Ri|\,\overline{uT} + \phi_{13} - \epsilon_{13}, \tag{13}$$

$$\frac{\mathrm{d}E}{\mathrm{d}t} = -S\,\overline{uw} + |Ri|\,\overline{wT} - \epsilon, \tag{14}$$

$$\frac{\mathrm{d}\overline{uT}}{\mathrm{d}t} = -s\,\overline{uw} - S\,\overline{wT} + \phi_{1T} - \epsilon_{1T}, \tag{15}$$

$$\frac{\mathrm{d}\overline{wT}}{\mathrm{d}t} = -s\,\overline{ww} + |Ri|\,\overline{TT} + \phi_{3T} - \epsilon_{3T}, \tag{16}$$

$$\frac{\mathrm{d}\overline{TT}}{\mathrm{d}t} = -2s\,\overline{wT} - \epsilon_{TT}. \tag{17}$$

Initially, the pressure correlations ϕ_{ij} and ϕ_{iT}, and the off-diagonal components of the dissipation rates ϵ_{ij} and ϵ_{iT}, are zero. The diagonal components are small because of the large Reynolds number. Thus, the initial trends of the solutions can be fully explained by means of the production terms which are linear in the shear S, the temperature stratification s and the Richardson number Ri. Only quadratic correlations are non-zero initially and contribute to the flow development. This explains the linear increase in the magnitude of $\overline{uw}$ and $\overline{wT}$. The vertical momentum flux is negative owing to the sign of its production rate. The vertical heat flux,

however, is negative (down-gradient) only for small Richardson numbers. If the Richardson number and the temperature fluctuations are large, the vertical heat flux may become positive. This means that turbulence transports heat vertically upwards from cold to warm regions in the fluid. This is the so-called 'counter-gradient heat-flux' (CGHF). A negative heat flux increases the temperature variance thus resulting in a change of sign of the correlation coefficient of $\overline{wT}$ for sufficiently large Richardson numbers even if the initial temperature fluctuations are small as displayed in figure 3. For $Ri = 0.5$ and 1, we observe such a CGHF. Its magnitude oscillates with a time period of about $\pi/(Ri)^{\frac{1}{2}}$ but persists different from zero.

The remaining correlations are controlled by the early development of the vertical momentum flux and vertical heat flux. These fluxes create a downstream heat flux $\overline{uT}$ in the presence of both shear and stratification despite the absence of an imposed mean temperature gradient in that direction. The correlation coefficient of $\overline{uT}$ increases monotonically for all positive Ri and approaches an asymptotic value of ~ 0.45. The downstream velocity variance depends only on the vertical momentum flux, which is always negative or, in the case of $Ri = 1$, almost vanishing for $t > 4$. The vertical velocity variance, however, depends on the sign of the vertical heat flux. Its sign change causes the observed trend of w' in figure 3(*c*). The lateral velocity would always decay unless it receives energy by the redistribution effect of the pressure–strain correlations.

It is clear that the initial trends of the correlations which result from the initial Gaussian fields cannot be compared directly with experimental data. However, the non-Gaussian characteristic of real turbulence develops quickly as will be shown in figure 4(*a*) below. Thus, we can compare the later results with observations. In the case of neutral stratification, $-\overline{uw}/(u'w')$ reaches a value of 0.5 which is very close to the values observed by Champagne *et al.* (1970), Harris *et al.* (1977) and Tavoularis & Corrsin (1981). The kinetic energy E/E_0 first decreases, reaches a minimum and then increases monotonically. In the experiment of Champagne *et al.* (1970) the increase was small because the wind tunnel was not large enough, but our results agree well with the measurements of Harris *et al.* (1977). Rohr *et al.*(1988) find that the turbulence intensities increase nearly linearly with time t. Although our simulation time is not large enough to support this finding quantitatively, the results are qualitatively consistent. The maximum value of the correlation coefficient $-\overline{wT}/(w'T')$ is 0.6 for weak stratification. Itsweire *et al.* (1986) determine maximum values of 0.5 for weakly stratified turbulence without shear. Tavoularis & Corrsin (1981) report a value of 0.45 and Budwig *et al.* (1985) find a value of 0.7–0.8 for very small Richardson numbers. Thus, the values of our computed correlation coefficients lie within the range of measurements although our turbulence Reynolds number is smaller than those of all cited experiments.

The temperature variance $\overline{TT}$ decays slowly for zero mean temperature gradient ($s = Ri = 0$), but increases strongly for weak stratification. Corresponding measurements are only available for very small Richardson numbers such that buoyancy effects could be neglected. Sirivat & Warhaft (1983) observed that the temperature variance first decreases and then increases. The rate of increase is large for large temperature gradients. In contrast, the experiments of Budwig *et al.* (1985) with transverse mean temperature gradients also at small Richardson number show only initially a moderate increase of temperature variance, while the variance becomes close to stationary further downstream in their wind tunnel. In the simulations, the strong increase of the temperature variance might be due to the larger Prandtl number which causes smaller thermal dissipation rates ϵ_{TT}. Thus, it is reasonable

that the trends in the simulations differ from those observed in wind tunnels. The temperature variance increases more strongly than the kinetic energy. This is another reason why the term $|Ri|\overline{TT}$ in (16) dominates after a short time and results in a decrease of $-\overline{wT}$ which eventually develops into a CGHF.

The down-gradient heat flux is typical for turbulence at neutral or weak stratification. A zero vertical heat flux in a stratified flow can be taken as an indicator of gravity-wave-like motion (Stewart 1969). The CGHF represents, however, an unusual flow state which requires further discussion. We shall come back to this aspect in §4. As suggested by Stewart (1969), Stillinger *et al.* (1983) and Itsweire *et al.* (1986), one may expect that the flow state changes from basically turbulent to more wave-like at the time when the negative vertical heat flux changes from maximum to minimum values. In the simulated flows, the periods when the flow changes character in this sense are $1 < t < 3$ for $Ri = 1$, and $1.2 < t < 4$ for $Ri = 0.5$.

3.2. *The quasi-steady state*

As discussed by Champagne *et al.* (1970), Harris *et al.* (1977) and Rohr *et al.* (1988) for cases with negligible buoyancy forces, the present flow will not achieve equilibrium. For neutral stratification, steady state would require a balance between shear production $-\overline{uw}\mathrm{d}U/\mathrm{d}z \approx c_p v^2 \mathrm{d}U/\mathrm{d}z$ and dissipation rate $\epsilon \approx c_\epsilon v^3/l$. The coefficients c_p and c_ϵ are approximately constants of order 0.5 for high Reynolds numbers. Thus, stationarity requires that the ratio $(c_p/c_\epsilon)\,Sh$ becomes unity, where Sh is the shear number defined in table 1. In our case, $Sh = 3.01$ so that shear production exceeds the dissipation rate. For stably stratified turbulence and very weak shear, the damping due to buoyancy and dissipation will dominate so that the turbulence decays. Only coincidentally, for a critical Richardson number, the shear production may just balance the dissipation terms. We have seen that the value of this critical Richardson number is about 0.1 for the present flow conditions. This value must be a function of the shear number because when the flow is close to steady state in neutral stratification, small buoyancy forces suffice to cause damping. On the other hand, the result of the linear theory, $Ri = 0.25$ (Miles 1961), is to be expected for $Sh \to \infty$. In our case, however, we are far from linearity and do not reach a stationary state.

A generalization of Batchelor's (1953) velocity-derivative skewness coefficient for anisotropic turbulence,

$$S_u = \frac{-\frac{1}{3}\sum_{i=1}^{3}\overline{(\partial u_i/\partial x_i)^3}}{\left[\frac{1}{3}\sum_{i=1}^{3}\overline{(\partial u_i/\partial x_i)^2}\right]^{\frac{3}{2}}}, \tag{18}$$

is a measure of the nonlinear energy transfer across the wavenumber space. Its time variation, depicted in figure 4(*a*), shows that this energy transfer is established at $t = 1$. It indicates a strong nonlinearity for neutral and weakly stable stratification, and reduced nonlinearity for $Ri \geqslant 0.5$. Figure 4(*b*) shows that the lengthscales increase initially, which is a consequence of the energy input due to shear at small wavenumbers and the energy loss due to dissipation at large wavenumbers. As the flow with large Richardson number develops, buoyancy forces suppress nonlinear turbulence interactions, causing the lengthscales to remain nearly constant and the skewness to diminish. In any case, the effects of shear and buoyancy cause deviations from a stationary state. This non-steady behaviour makes it difficult to obtain any conclusive results from the simulations or corresponding experiments.

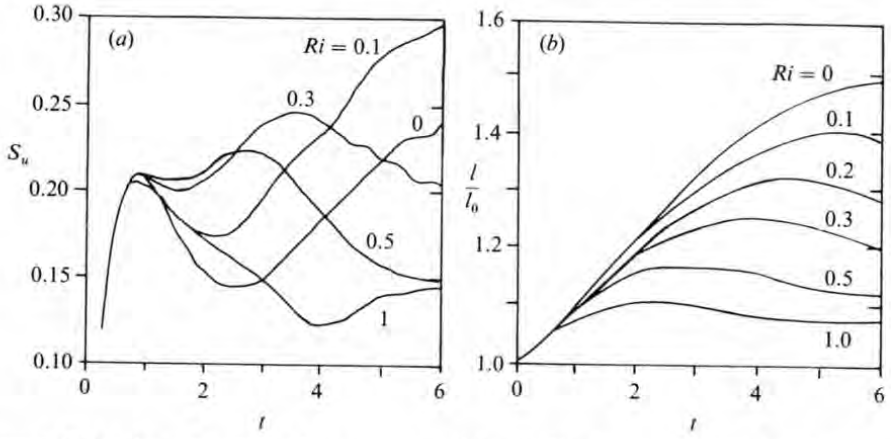

FIGURE 4. Velocity-derivative skewness S_u and normalized integral lengthscale l/l_0 versus time for various Richardson numbers Ri.

Fortunately, however, we can expect to achieve a 'quasi-steady' or 'asymptotic' state, in which all turbulence correlations properly normalized with the actual r.m.s. velocity and temperature fluctuations become nearly constant. The quasi-steady state could be reached *exactly* if the lengthscale were to become constant (which is indeed the case for $Ri \geqslant 0.5$). Then, the dissipation rates (and also the correlations of pressure–strain and pressure–temperature gradient) become a linear function of the turbulence variances. Thus, (10)–(17) become a homogeneous linear system with seven linearly independent equations. Such a linear system has eigensolutions with complex eigenvalues. The imaginary parts of the eigenvalues are related to the dimensionless Brunt–Väisälä frequency $N = |Ri|^{\frac{1}{2}}$ of free vertical oscillations in a stratified fluid. The buoyancy forces couple $\overline{ww}$ with $\overline{wT}$ and $\overline{uw}$ with $\overline{uT}$ so that four oscillating modes with two pairs of complex-conjugate eigenvalues are to be expected. The real parts are due to the inverse timescales of production minus dissipation rates. Their magnitudes are larger than the Brunt–Väisälä frequency for large shear numbers. After some time, the eigensolution corresponding to the eigenvalue with maximum real part dominates relative to all other eigensolutions and then all solution components are proportional to the components of the corresponding eigenvector so that their ratios are constants. Schumann (1987) has applied a second-order closure model for (10)–(17) and computed the corresponding eigensolutions numerically. He found, as expected, that for the parameters corresponding to the present case, only one eigensolution with maximum real part of the eigenvalue exists and this eigenvalue is purely real. In addition, two pairs of complex-conjugate eigenvalues arise with smaller real parts. Thus, even for non-constant slowly changing lengthscales we can in fact expect to find a quasi-steady state in which the normalized turbulence correlations vary only as fast as the integral turbulence lengthscale does.

The difference between the largest and the second largest eigenvalue controls the time required to achieve the quasi-steady state. The present system has seven complex eigenvalues. For an order of magnitude estimate we may assume that the real parts of the eigenvalues are equidistantly distributed between zero and the maximum value. Thus we expect to achieve the quasi-steady state after a time of order $7\epsilon/E \approx 7\nu/l = 7/Sh \approx 2.4$. Figure 3 indicates that this estimate is only little smaller than the actual value, and the correlations remain almost constant after a

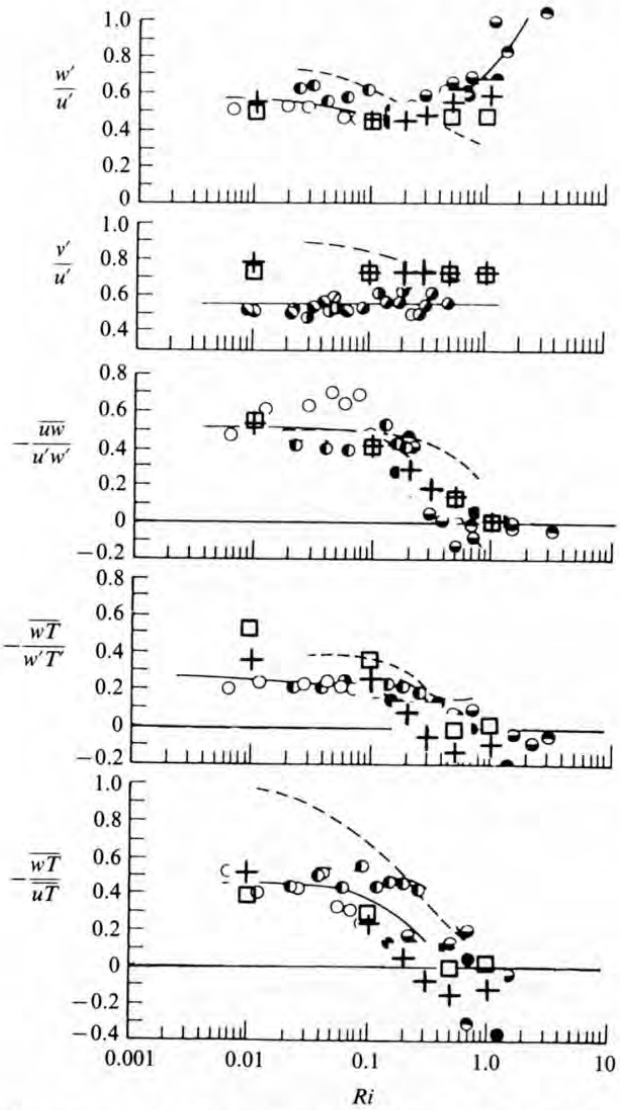

FIGURE 5. Turbulence quantities versus gradient Richardson number. The experimental data of Komori *et al.* (1983) in water are shown by circles (○, ◒, ●) and by approximate interpolation (full curve). The dashed curve represents Webster's (1964) measurements in air. The simulation results are indicated by crosses (+) for $Pr = 5$, and by squares (□) for $Pr = 0.7$ at $t = 4.5$.

time of about 3.5. We have also performed simulations with 32 grid points in each direction over much longer times (up to $t = 24$) which confirmed the quasi-steady state and showed for $Ri = 1$ that $\overline{wT}$ stays definitely positive while $\overline{uw}$ oscillates with small and decreasing amplitude around zero (Schumann *et al.* 1986).

3.3. *Comparison with Komori et al.'s measurements* ($Pr = 5$)

In this section we discuss Komori *et al.*'s (1983) measurements and the simulation results for $Pr = 5$. We assume that the experiment is in quasi-steady state at the position of the measurements. For $Ri = 1$, we achieved the best agreement with the measurements at $t = 4.5$. Thus, we compare the results of all simulations at this time, which is close to the final time of our simulation, with the experimental results. Figure 5 compares different measured and simulated turbulence quantities for flows

with $Ri = 0.01, 0.1, 0.2, 0.3, 0.5$, and 1. Both the experiment and simulation show that with increasing Richardson number the ratio of the r.m.s. values of the vertical and the downstream velocity fluctuations $w'/u' = (\overline{ww})^{\frac{1}{2}}/(\overline{uu})^{\frac{1}{2}}$ decreases for weakly stable stratification. But this trend reverses, becoming one of increasing w', if the flow is strongly stably stratified. The ratio of the lateral and the downstream r.m.s. velocities v'/u' remains unaffected by the variations of Ri. For this ratio, the experimental values are about 20% lower than the simulations. A second-order closure model predicts about the same difference between model results and the measurements (Schumann 1987). The reason may be that in the experiment the lateral velocity fluctuations are smaller than they would be in an infinitely wide channel. The lateral boundaries of the channel are the only means by which the flow in this direction is influenced and may result in smaller values of v'. The alternative that the models underestimate the energy redistribution by the pressure–strain correlation ϕ_{22} is less likely because it would also affect the two other velocity components which exhibit reasonable agreement with the measurements. Figure 5 shows further that the negative correlation coefficients of the vertical fluxes of momentum and heat, both in the experiment and in the simulations, vanish and then change sign for $Ri \geqslant 0.5$ and that the ratio of the vertical and the downstream heat fluxes always remains smaller than unity, i.e. $\overline{uT}$ is larger than $\overline{wT}$ for all stable stratifications. In summary, the agreement between measured and simulated results is qualitatively and quantitatively very good and supports the validity of the simulations for the present case.

3.4. *Simulation of an air flow* ($Pr = 0.7$)

In this section we compare two simulated flows with different molecular Prandtl numbers, $Pr = 0.7$ (air) and 5 (water). We use the same physical and numerical initialization parameters as above, see table 1. We achieve the same results qualitatively as Webster's (1964) wind-tunnel measurements: figure 5 illustrates that the negative turbulent vertical heat flux in the quasi-steady flow at $t = 4.5$ approaches zero but never changes sign even for strong thermal stability, $Ri \geqslant 0.5$. This coincides with Webster's data, shown as a best-fit curve in figure 5, who also observed no positive heat fluxes $\overline{wT}$. The ratio of vertical and downstream heat fluxes corroborates this result.

Interestingly, the ratio of vertical and downstream r.m.s. velocity is rather insensitive to Ri for $Pr = 0.7$, whereas the correlation coefficients of the vertical momentum fluxes of high and low Prandtl-number flows are almost indistinguishable. The computed results for v'/u' for $Pr = 0.7$ agree much better with Webster's data than do the corresponding values for $Pr = 5$ with Komori's results. This further supports our conclusion that the small values reported by Komori *et al.* (1983) may be induced by sidewall effects.

3.5. *Rates of dissipation*

Here, we shall discuss further the results for $Pr = 5$. The velocity and temperature fluctuations have been initialized isotropically, and therefore the initial values of the mechanical and thermal rates of dissipation differ by the value of the Prandtl number: $\epsilon_0 = \epsilon_{ii_0}/2 = 3\epsilon_{11_0}/2 = 3Pr\epsilon_{TT_0}/2$. Thus, for $Pr = 5$, the initial value of ϵ_{TT} is approximately one order of magnitude smaller than the kinetic energy dissipation rate.

Figure 6 shows the time variation of the dissipation rates as they develop in manners similar to those of the kinetic energy and the temperature variance

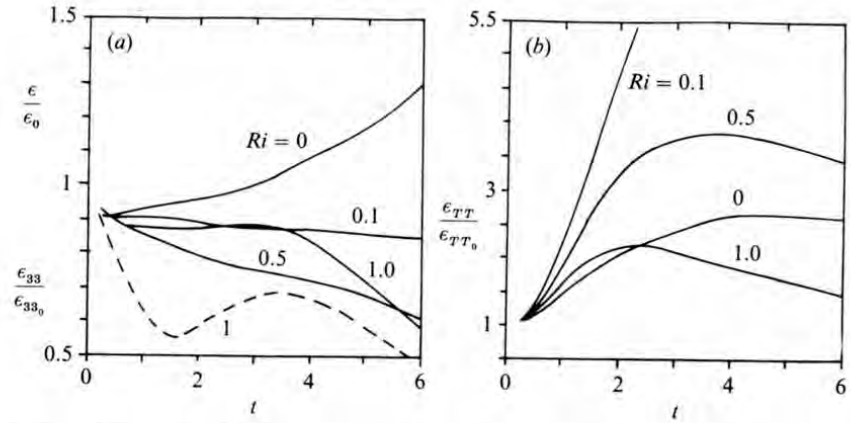

FIGURE 6. Viscous and thermal dissipation rates versus time. (*a*) —, ϵ/ϵ_0; ——, $\epsilon_{33}/\epsilon_{33_0}$ for $Ri = 1$; (*b*) $\epsilon_{TT}/\epsilon_{TT_0}$. Note the different scaling of the ordinate axes.

respectively, compare figure 3(*a*, *b*). For $Ri = 0$, the initial trends of both the mechanical and thermal dissipation rates reflect the effect of inertial-convective energy transfer from small to large wavenumbers. Increasing Richardson number decreases the mechanical dissipation rate because of buoyancy damping which acts at all scales. The thermal dissipation rate increases strongly because of the excitation of small-scale temperature fluctuations by the heat flux. For strong stability, however, the trends change: the maximum value of ϵ_{TT} at $Ri = 1$ is less than that at $Ri = 0.5$, whereas ϵ is larger at $Ri = 1$ than at $Ri = 0.5$.

It is noteworthy that, for $Ri = 1$, the increase of the mechanical dissipation rate in the time period $2 \leqslant t \leqslant 4$ originates mainly from ϵ_{33}, i.e. from vertical motions, see the dashed curve in figure 6(*a*). Thus, we expect that the CGHF is correlated with fine-scale motion which is turbulent even at high Richardson numbers, at least in this intermediate time period. Similar observations have been reported by Riley *et al.* (1981) from simulations of unsheared stratified turbulence. On the other hand, we also notice a CGHF for $Ri = 0.5$, see figure 3(*f*), but without any remarkable increase of ϵ. In this case of moderate stratification, the CGHF occurs late, at $t \approx 4$ when the turbulence dynamics have already been reduced considerably (compare w' for $Ri = 0.5$ and 1 in figure 3*c*). The reason for that is basically the relative importance of production of kinetic energy and damping of temperature variance at small scales due to buoyancy forces. Note that for $Ri \geqslant 0.5$ and $t > 4$, the decay of the thermal dissipation rate is weaker than the decay of the mechanical dissipation rate. This is a consequence of the large Prandtl number, for which velocity fluctuations are damped out more quickly than temperature fluctuations. Thus, the final state of turbulence at high Richardson and Prandtl numbers exhibits dynamically inactive and small-scale temperature fluctuations.

3.6. *Anisotropy*

Shear and buoyancy forces acting on isotropic turbulence cause depature from isotropy such that turbulence kinetic energy will be distributed unequally among the velocity components. The anisotropy tensor is commonly defined as

$$b_{ij} = \frac{\overline{u_i u_j}}{\overline{u_k u_k}} - \tfrac{1}{3}\delta_{ij}. \tag{19}$$

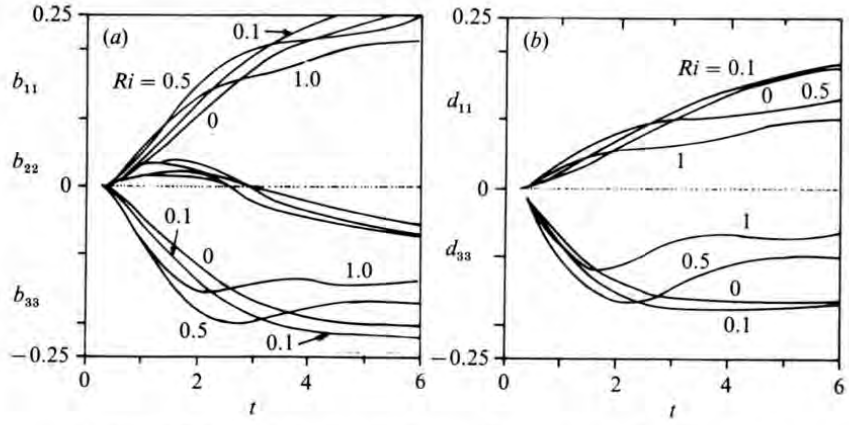

FIGURE 7. Normalized anisotropy of stresses and dissipation rates.

Figure 7(*a*) depicts the diagnonal components of this tensor for $Pr = 5$. Launder (1975) postulated an increase of the absolute values of b_{11} and b_{33} with increasing Ri. The direct simulations, however, confirm this only for weakly and moderately stable stratification ($0 < Ri < 0.5$). When the flow has reached a quasi-stationary state, the components of the anisotropy tensor for $Ri \geqslant 0.5$ are significantly smaller than those for $Ri = 0$ or 0.1. The anisotropy components in the downstream and vertical direction have larger magnitude and opposite signs, whereas $b_{22} = -(b_{11} + b_{33})$ is much smaller and insensitive to Ri. Figure 5 indicates that $w'/u' < 1$ and thus $|b_{33}| < b_{11}$. Both the measurements of Komori *et al.* and our simulations show that a strong thermal stability reduces the anisotropy of the flow, which might be a rather unexpected behaviour but is explainable as discussed in §3.1.

The anisotropy tensor of the dissipation rate can be calculated from

$$d_{ij} = \frac{\epsilon_{ij}}{2\epsilon} - \tfrac{1}{3}\delta_{ij}. \tag{20}$$

The correlations d_{11} and d_{33} are plotted in figure 7(*b*). The anisotropy of the dissipation tensor develops qualitatively in the same manner as the anisotropy of the Reynolds stresses. It is surprising that the magnitude of the dissipation anisotropy is only a little smaller than that of the stresses. At high Reynolds numbers, one expects locally isotropic turbulence with isotropic dissipation rates. Here, however, the turbulence intensity is restricted to moderate values of Re owing to the restricted numerical resolution. For this reason, the dissipation is directly influenced by the low-wavenumber parts of the spectrum, which is anisotropic. This however is only one reason for the anisotropic values of the dissipation tensor. Another is that shear and buoyancy forces create anisotropy even at the small scales. Note that the anisotropy of the dissipation tensor tends to reduce the anisotropy of the stresses and thus supports the isotropizing effect of the pressure–strain correlations, see §5 below.

3.7. *Turbulent Prandtl number*

The turbulent Prandtl number is the ratio of the turbulent diffusivities of momentum and heat. In the normalized form used here it reads

$$\sigma_t = \frac{\overline{uw}\,s}{\overline{wT}\,S}. \tag{21}$$

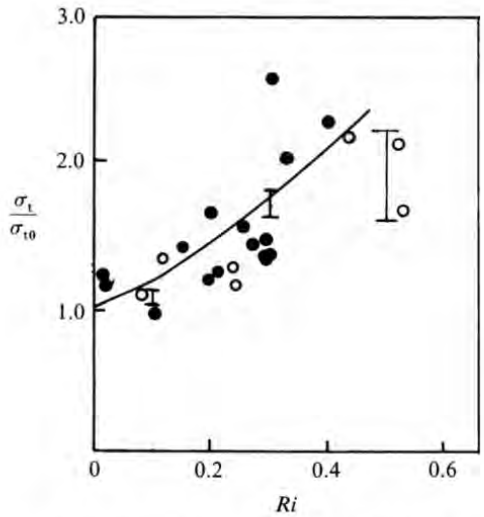

FIGURE 8. Turbulent Prandtl number normalized with its value for neutral stratification versus gradient Richardson number. Experimental data by Webster (1974) (●, ○), data obtained from Launder's model (1975) (—) and results from direct numerical simulations (with error bars) for $Pr = 0.7$. The error bars reflect the scatter of the numerical results in the time interval $5.5 \leqslant t \leqslant 6$.

In figure 8 the turbulent Prandtl number, obtained from the simulation of an air flow ($Pr = 0.7$), is plotted versus Richardson number. The values are normalized by σ_{t0}, which is the value of σ_t for $Ri = 0$. Our result for this reference value is 0.79 ± 0.01 in the time interval $5.5 < t < 6.0$. Webster (1964) measured much smaller values for σ_{t0}, varying between 0.15 and 0.3. Tavoularis & Corrsin (1981) measured values between 1.06 and 1.12 for this turbulent Prandtl number. Launder (1975) adjusted his second-order closure model to other data of Webster (1964) and obtained $\sigma_{t0} = 0.63$. The normalized turbulent Prandtl number increases with Richardson number because buoyancy suppresses heat flux more than momentum fluxes. It becomes infinite when the heat flux vanishes. This is the case for a Richardson number of order 0.5 in our simulations for both $Pr = 5$ and 0.7. The singularity near $Ri = 0.5$ explains the growing scatter of the results with increasing Richardson number when $\overline{wT}$ diminishes and approaches zero. The general trend is equally predicted by Webster (1964), Launder (1975) and by our simulations.

4. The physics of the counter-gradient heat flux (CGHF)

In the previous sections, we have shown that a persistent CGHF arises for strong stratification if the Prandtl number is sufficiently large. CGHFs have also been observed for stably stratified homogeneous turbulent flows without shear in the water experiments of Itsweire *et al.* (1986) and in the corresponding direct simulations of Riley *et al.* (1981). Deardorff (1966) and Schumann (1987) show that CGHF also arises in stably stratified parts of buoyancy-induced inhomogeneous turbulence. We have explained this phenomenon in terms of (16) which implies a positive production rate of the heat flux counter to the mean temperature gradient if $|Ri|\overline{T'T'}$ is larger than all other source or sink terms in this equation. In this section, further properties of the CGHF will be explained and compared to the findings of Komori *et al.* (1983).

Down-gradient heat flux corresponds to positive mean temperature gradient and

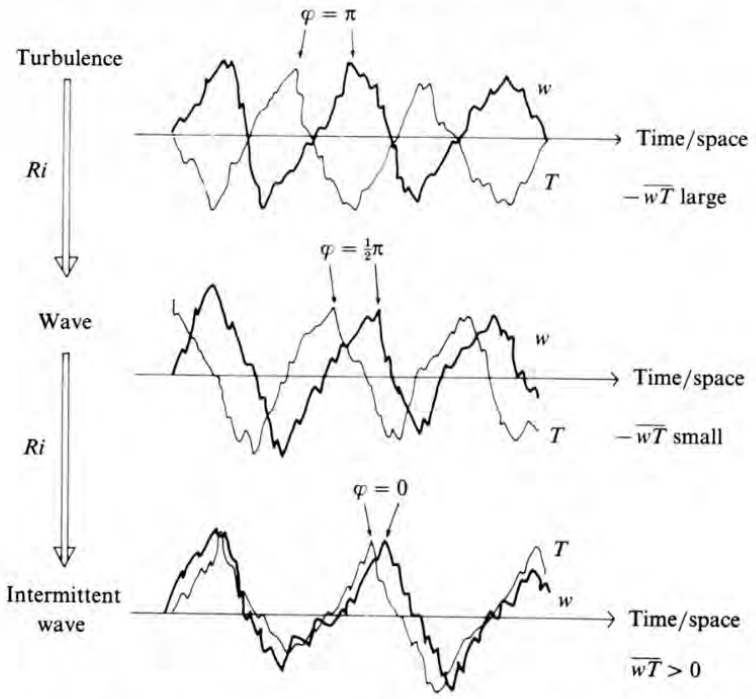

FIGURE 9. Turbulence and wave characteristics for stable stratification. The sketches of signals of w (thick curves) and T (thin curves) illustrate typical phase angles φ according to the Richardson number which increases from top to bottom. (Adapted from Komori *et al.* 1983.)

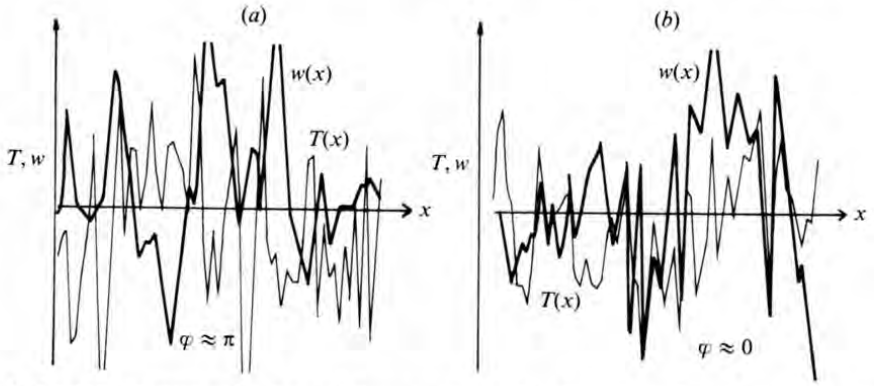

FIGURE 10. Instantaneous velocity and temperature signals versus downstream coordinate x as computed for $t = 4$, and $y = 0.5, z = 0$ with (*a*) $Ri = 0$ and (*b*) $Ri = 1$. The signals show the expected phase angles.

negative correlations of $\overline{wT}$ and, hence, implies a mean phase angle φ of order π as sketched in figure 9. If the phase angle decreases to $\pi/2$ the heat flux vanishes. A phase angle of order $\pi/2$ implies that $\partial w/\partial t$ and T are in phase and this is typically the case for gravity waves (Stewart 1969). If the phase angle decreases further and approaches zero, the heat flux changes sign and becomes positive. Komori *et al.* (1983) call this state 'intermittent waves'. Figure 10 shows signals $w(x)$ and $T(x)$ at time $t = 4$ as computed from the direct simulations. Although the phase angles exhibit considerable scatter, the results for $Ri = 0$ and 1 clearly corroborate the observed change in phase angle from $\varphi \approx \pi$ to $\varphi \approx 0$. Figure 10 (*b*) also illustrates that

the phase angle is zero in particular with respect to high-wavenumber components of the signal. This fact is confirmed quantitatively by velocity–temperature cross-spectra (Gerz 1988*a*), which show clearly that the heat transfer is positive for $Ri = 1$ in particular at high wavenumbers, while it is negative or zero for small wavenumbers. This behaviour is to be expected from the increasing ratio of temperature fluctuations to velocity fluctuations with increasing wavenumber because of the weaker dissipation rate of temperature fluctuations at this rather large Prandtl number. The dissipation rates, see figure 6, reflect these facts. High-frequency components of the CGHF cause an increase of the dissipation rate for kinetic energy while they reduce the dissipation rate of temperature variance.

For strongly stable stratification, Komori *et al.* (1983) found that the gravity waves dominate the large scales, and are superimposed by turbulent 'hot eddies' at the small scales. We prefer to call the 'hot eddies' 'hot active *cells*' as long as they are mixed by the turbulence and 'hot inert *spots*' when the velocity fluctuations are almost damped out. This seems to be a more suitable nomenclature for what happens in such flows.

Komori *et al.* (1983) report that the 'hot cells' are advected from upstream by the mean flow where they originate owing to the interaction of the velocity fluctuations with the strong positive temperature gradient in the upper part of the channel. In the simulations with periodic boundaries and with zero-mean advection, the hot cells cannot be generated upstream, rather they must be formed locally or in the past. In order to demonstrate that this is in fact the case, we discuss instantaneous fields of vertical velocity, temperature and heat-flux fluctuations at various Richardson numbers and times.

In figure 11 horizontal cross-sections of the three-dimensional field of the vertical heat flux are plotted at different times for $Ri = 0.1$ and 1. The initial values prescribe isotropic fields and thus zero mean vertical flux. This can be verified from the plot for $t = 0$ where the number of positive and negative local heat fluxes is approximately equal. For moderate Richardson number ($Ri = 0.1$), the areas with locally negative heat fluxes grow with time, and so does the mean, see figure 3(*f*). For $Ri = 1$ and $t = 2$, the distribution of heat flux looks much the same as at $t = 0$, i.e. the mean of wT vanishes again. This agrees with the temporal development of $\overline{wT}$ reported in figure 3 where the heat flux changes sign at about $t = 2$. At time $t = 4$, however, areas with positive local heat fluxes predominate as seen in figure 11. Obviously, the positive heat flux is carried by relatively small-scale cells.

Our results differ from those of Komori *et al.* (1983) in that we observe not only hot rising cells ($w > 0$, $T > 0$) but also, equally often, cold descending parcels ($w < 0$, $T < 0$), all contributing to the positive heat flux. This is illustrated in figure 12 where horizontal cross-sections of the fields of the instantaneous vertical velocity and the temperature fluctuations are plotted separately for $Ri = 1$ at time $t = 4$. Negative deviations from the reference values occur as frequently as positive ones. In the simulations, this result is to be expected because of symmetrical linear external forces. In the laboratory experiment, however, the temperature profile is nonlinear, $\mathrm{d}^2T_0/\mathrm{d}z^2 > 0$, and thus causes a positive skewness of the distribution of the temperature fluctuations, $S_T \equiv \overline{TTT}/(\overline{TT})^{\frac{3}{2}} > 0$, with few, but strongly positive, and many, but weakly negative, deviations from the mean temperature. The velocity reacts to this skewness due to buoyancy forces in a similar manner so that hot ascending cells prevail in the experiment.

Thus the present flow with strong stratification and large Prandtl number and moderate Reynolds number provokes a process that creates cold and hot, locally

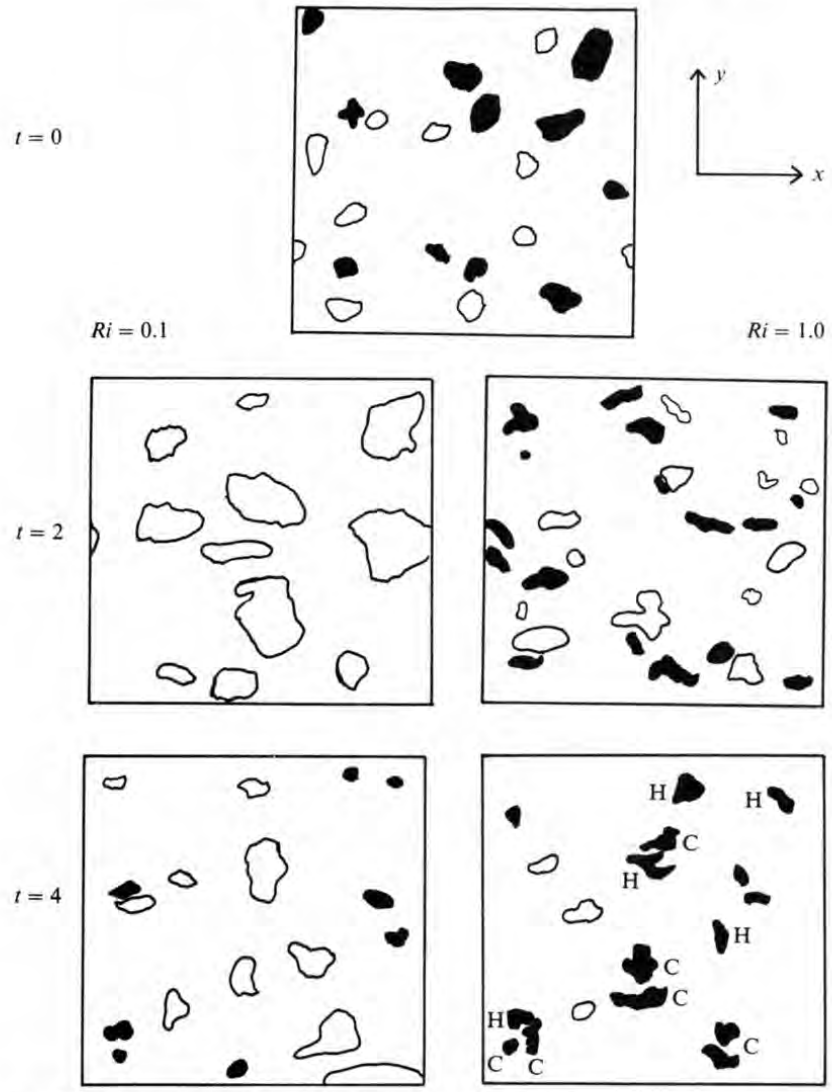

FIGURE 11. Spatial distribution of local vertical heat fluxes wT in horizontal cross-sections at $z = 0$ and $t = 0$, 2 and 4 for $Ri = 0.1$ (left) and $Ri = 1$ (right). White/black areas indicate negative/positive heat fluxes with absolute values larger than 0.0004. For $Ri = 1$ and $t = 4$ the hot ascending cells are marked H and the cold descending cells are marked C.

isolated small turbulent cells at places where the initial temperature possesses corresponding extreme values. These small buoyancy-driven cells with locally positive heat flux modulate larger gravity waves with zero heat flux which have been generated in the stable environment. Buoyancy forces suppress vertical motions so that the turbulence gradually degenerates towards a two-dimensional state. If $Pr > 1$, the thermal fluctuations have a longer 'lifetime' and hence the two-dimensional cells become dynamically inactive hot and cold spots in the wavy flow. This is the situation that Gibson (1987) calls 'fossil turbulence'.

As discussed by Riley *et al.* (1981), the CGHF converts available potential energy $E_{\text{pot}} = Ri\overline{TT}/2$ (Gill 1982) into kinetic energy of the velocity fluctuations $E = \overline{u_i u_i}/2$. This can be seen from (14) and (17). In fact, if we form the total energy as the sum of potential energy E_{pot} and kinetic energy E, we see that the total energy is

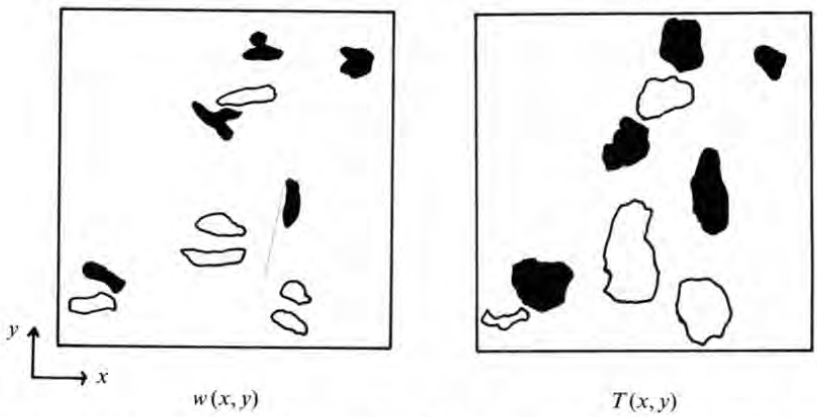

FIGURE 12. Spatial distribution of vertical velocity w and temperature T in horizontal cross-sections at $z = 0$ and $t = 4$ for $Ri = 1$. The white/black areas represent negative/positive deviations from the mean with absolute values larger than 0.01. They correspond to those in figure 11 marked with C and H, respectively.

invariant with respect to the heat flux. Thus, the CGHF is consistent with energy conservation. In contrast to the results of Riley *et al.* (1981) and Hunt *et al.* (1988), who applied the rapid distortion theory to the development of stratified sheared and unsheared homogeneous turbulent flows, the CGHF observed in our simulations does not oscillate around zero but keeps its sign. The oscillations are a consequence of the initial imbalance between kinetic and available potential energy and thus occur at all scales with a time period of $\approx \pi/N$, where N is the Brunt–Väisälä frequency. The persistent positive heat flux reflects the imbalance of dissipation of kinetic and potential energy and is thus a consequence of small-scale motions.

Note that for a steady-state flow without diffusional or external sources of temperature variance, the heat must flow down gradient as can be seen from (17), because only then can the production term balance the positive thermal dissipation rate. Thus the CGHF is a property of a flow in which the temperature variance (potential energy) is locally in non-equilibrium. In fact, the CGHF is necessary to achieve a quasi-steady state: in the quasi-steady state, the ratio of potential to kinetic energy should stay constant. In the present case, the temperature fluctuations and thus potential energy are only weakly dissipated by conductivity because of the rather large Prandtl number and moderate Reynolds number. Thus the dissipation rate of temperature variance is too small to produce the same rate of decay as the viscous dissipation does for kinetic energy. In the absence of heat flux, this condition would cause a non-steady ratio of potential to kinetic energy. Thus, the CGHF becomes necessary to restore the quasi-steady state.

As a consequence of this explanation, we conclude that a CGHF arises if velocity fluctuations in stably stratified flows create large amounts of potential energy and if the dissipation rate of temperature variance is too small to produce the same decay rate as that of kinetic energy. The imbalance is to be expected in particular for large-Prandtl-number flows such as water. This explains the appearance of CGHF in the experiments of Komori *et al.* (1983) and Itsweire *et al.* (1986) while it does not occur in the air flow experiment of Webster (1964). Alternative reasons for the imbalance of potential energy relative to kinetic energy are initial conditions which produce relatively large temperature fluctuations in strongly stratified flows. The CGHF in the inhomogeneous boundary layers discussed by Deardorff (1966) and Schumann

(1987) are produced by large diffusive sources of potential energy which are not balanced by thermal dissipation.

In summary, the CGHF can be explained by basically linear processes. Nonlinear effects modify the phenomenon but they do not cause the occurrence of the CGHF. This is corroborated by the results of Hunt *et al.* (1988). At high Reynolds numbers, the dissipation rates for temperature and velocity fluctuations will be less sensitive to molecular diffusivities so that the present form of a weakly oscillating but persistent positive heat flux (CGHF) is likely to be a feature of moderate-Reynolds-number flows only. This has been confirmed by means of the second-order closure model described in Schumann (1987) as reported in Gerz (1988*a*).

5. Closure modelling and proposal for improvements

5.1. *Pressure correlations and closure models*

Correlations of the pressure–strain ϕ_{ij} and the pressure–temperature gradient ϕ_{iT} occur in the equations of the Reynolds stresses, (10)–(13), and the heat fluxes, (15) and (16). In second-order models, these terms must be modelled to close the equations as proposed by Launder (1975, 1976) and Zeman & Lumley (1976) for stratified flows with small to moderate Richardson numbers. Here, the validity of such models will be investigated for the case where the stability is high ($Ri = 1$) and improvements will be suggested. Direct simulation suits this purpose because pressure fluctuations transfer energy between Fourier modes at wavenumbers of comparable magnitude which can all be resolved by the simulations. This contrasts with the nonlinear energy transfer from small to large wavenumbers which controls the dissipation rates but requires higher numerical resolution.

In a stratified shear flow the correlations

$$\phi_{ij} = \overline{p\left(\frac{\partial u_i}{\partial x_j}+\frac{\partial u_j}{\partial x_i}\right)}, \qquad \phi_{iT} = \overline{p\frac{\partial T}{\partial x_i}}, \tag{22a, b}$$

are composed of three contributions

$$\phi_{ij} = \phi_{ij_1}+\phi_{ij_2}+\phi_{ij_3} \qquad \phi_{iT} = \phi_{iT_1}+\phi_{iT_2}+\phi_{iT_3}. \tag{23a, b}$$

The contribution to ϕ_{ij} are the turbulent–turbulent (Rotta) term ϕ_{ij_1}, the production term due to mean shear ϕ_{ij_2} and the production term due to buoyancy ϕ_{ij_3}. Corresponding models (Launder 1976) are

$$\phi_{ij_1} = -c_1\frac{\epsilon}{E}(\overline{u_iu_j}-\tfrac{2}{3}E\delta_{ij}), \tag{24}$$

$$\phi_{ij_2} = -c_2(-\overline{u_iu_k}S_{jk}-\overline{u_ju_k}S_{ik}+[\tfrac{2}{3}\overline{u_lu_k}S_{lk}]\,\delta_{ij}), \tag{25}$$

$$\phi_{ij_3} = -c_3(|Ri_j|\overline{u_iT}+|Ri_i|\overline{u_jT}-[\tfrac{2}{3}|Ri_l|\,\overline{u_lT}]\,\delta_{ij}). \tag{26}$$

Here, we have introduced a vectorial Richardson number associated with a gravity vector ($|Ri_l| = |Ri|\delta_{l3}$) and a shear tensor ($S_{lk} = S\delta_{l1}\delta_{k3}$) to complete the equations, and c_1, c_2, c_3 are the model coefficients.

Figure 13(*a*) illustrates the development of $\phi_{11}, \phi_{22}, \phi_{33}$ and ϕ_{13} with time for strong stratification ($Ri = 1$). The correlations are calculated from the simulated results of turbulent velocity and pressure as defined in (22*a*). The pressure–strain terms act to reduce the anisotropy of the flow. Initially the shear creates large values of $\overline{uu}$ and therefore ϕ_{11} is negative and distributes the energy from the downstream to the

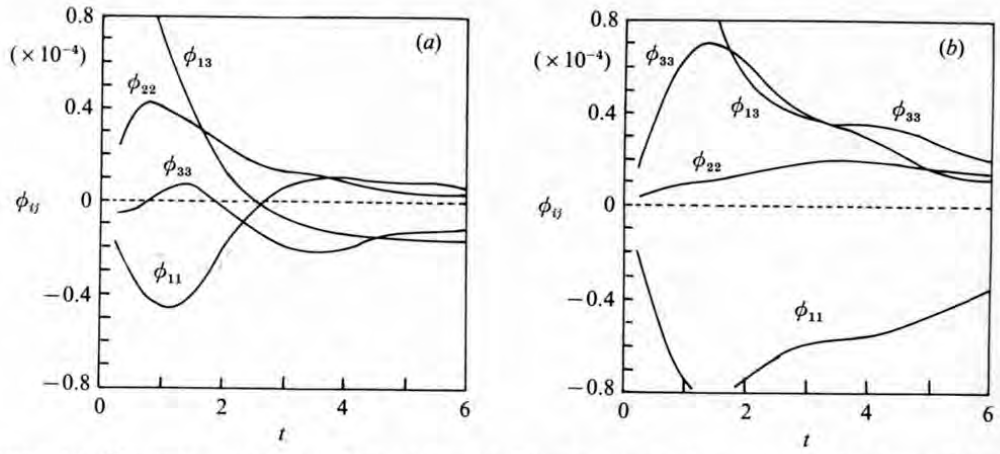

FIGURE 13. Pressure–strain correlations ϕ_{ij} for $Ri = 1$ versus time. (*a*) Results from the direct simulation with (22*a*); (*b*) results of the closure model (23*a*); (24)–(26) with the coefficients $c_1 = 2.0$, $c_2 = 0.6$ and $c_3 = 0.3$.

	c_1	c_1^*	c_2	c_3	c_3^*
Launder (1985), Zeman & Lumley (1976)	2.0		0.6	0.3	
Weinstock (1986)	0.6	0.5	0.6	0.3	0.6
Best results for $Re_\lambda \approx 25$ and $Ri = 1$	0.1		0.6	0.6	

TABLE 2. Model coefficients of the ϕ_{ij}

lateral and vertical components of the normal stresses. In phase with $\overline{uw}$, ϕ_{11} reaches its minimum values at $t \approx 1.3$. Components ϕ_{22} and ϕ_{33} are positive in this period and act as source terms for $\overline{vv}$ and $\overline{ww}$. Note that the trace ϕ_{ii} must vanish identically owing to continuity. The term ϕ_{22} is larger than ϕ_{33} because the lateral stress component receives more kinetic energy than the vertical one owing to the buoyancy effect.

The situation is reversed at a later time when $\overline{wT}$ changes sign and becomes a CGHF. Then the positive heat flux creates dominating vertical motions $\overline{ww}$ causing a sign change of ϕ_{11} and ϕ_{33} in the interval $1.8 < t < 2.7$ during which the CGHF reaches its maximum value. The component ϕ_{33} is negative and reaches its maximum magnitude at this time, and redistributes the kinetic energy in almost equal shares to the downstream and the lateral stress components which have positive pressure–strain terms.

The positive ϕ_{13} acts as a sink for $-\overline{uw}$; ϕ_{13} decreases with $-\overline{uw}$. The former changes sign at $t \approx 2.5$ to counteract the strong decay of the momentum flux, see figure 3(*d*). Thus, the evolution of the pressure–strain correlation reflects the change from shear- to buoyancy-dominated turbulence. In the quasi-stationary state of the flow, buoyancy dominates and causes $\phi_{33}, \phi_{13} < 0$ and $\phi_{11} > 0$.

For comparison, the behaviour of the pressure–strain terms as predicted by the models (24)–(26) is depicted for the same case in figure 13(*b*). These results are obtained using the values of the coefficients c_1, c_2 and c_3 proposed by Launder (1975) and Zeman & Lumley (1976), see table 2.

The result of the closure model differs considerably from the result of the direct

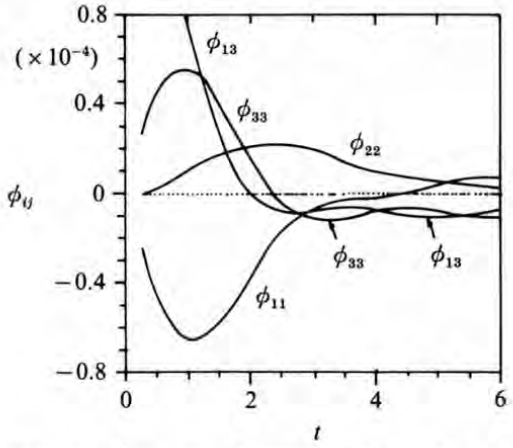

FIGURE 14. Best results for closure modelling ϕ_{ij}. Same data as in figure 13(*b*) (but with the coefficients $c_1 = 0.1$, $c_2 = 0.6$ and $c_3 = 0.6$.

simulation. The closure model predicts values that are about double the magnitude of those of the simulation. Part of this difference is because the closure model assumes isotropic dissipation while the simulations exhibit strongly anisotropic dissipation rates, see Figure 7(*b*), which contribute to the isotropizing effects. This is certainly a feature of the rather small turbulence Reynolds number of our simulation. More importantly, the closure model fails to describe the change in sign of ϕ_{11} and ϕ_{22}. By considering the individual contributions of the various model components, we found that the reason for these discrepancies is mainly the overestimation of the turbulent–turbulent interaction. Stratification acts to reduce the 'collisions' between flow parcels. These collisions constitute the basic physical mechanism of the turbulent–turbulent interaction. Moreover, the model underestimates the redistribution of buoyancy sources, i.e. c_3 is too small.

Much better agreement is achieved if c_1 is reduced to 0.1 and if c_3 is increased to 0.6, as shown in figure 14. The coefficient c_2 has been kept unchanged. With these coefficient values the model correctly describes the sign changes of ϕ_{11}, ϕ_{33} and ϕ_{13} and predicts the same magnitude as the direct simulation results at the final time.

Launder (1975) deduced the value of 0.6 for the coefficient c_3 by adjusting the model results to the data of Webster (1964). Zeman & Lumley (1976) determined the value $c_3 = 0.3$ for isotropic turbulence. Weinstock (1986) deduced analytically that in stably stratified flows the turbulent–turbulent interaction is reduced by stratification. This corresponds to a reduced value c_1^* instead of c_1 (see table 2) and an additional buoyancy term which can be combined with ϕ_{ij_3} thus resulting in a new coefficient $c_3^* = 0.6$ which confirms Launder's empirical value. Weinstock (1986) points out that the turbulent–turbulent term reduces the rate of growth of anisotropy rather than causing a return to isotropy. The direct simulation results confirm this conclusion and show that the influence of ϕ_{ij_1} is almost negligible in flows with strongly stable stratification.

The direct numerical simulation results for the pressure–temperature gradient correlations ϕ_{iT} defined in (22*b*) are plotted in figure 15(*a*) for the same Richardson number, $Ri = 1$. The lateral component ϕ_{2T} is non-zero only because of statistical uncertainties due to the limited data from which the mean values are computed. The horizontal component ϕ_{1T} is also small but reflects the change from a shear- to

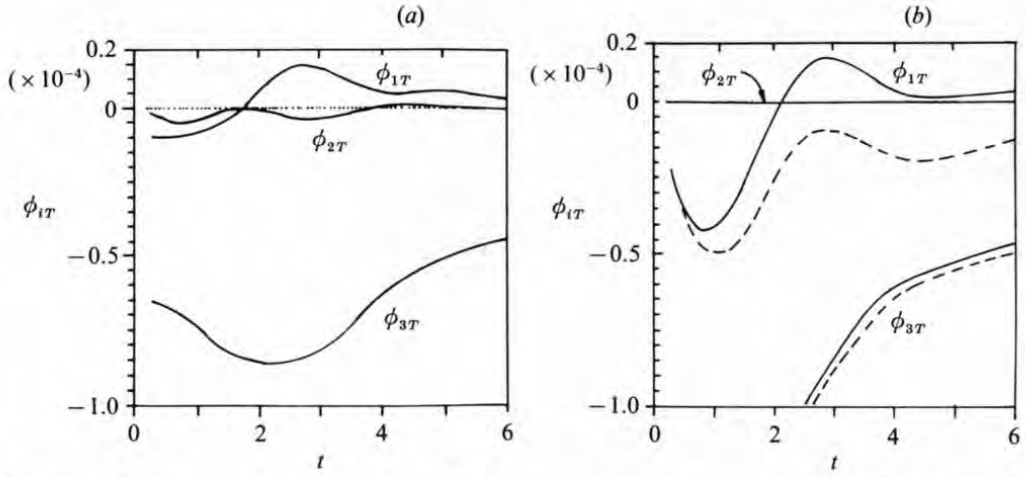

FIGURE 15. Pressure–temperature gradient correlations versus time for $Ri = 1$. (*a*) Results evaluated from the simulations according to (22*b*); (*b*) results obtained from the model equations (27)–(29) with the coefficients $c_{1T} = 1.05$, $c'_{1T} = 0.05$, $c_{2T} = 0.96$, $c'_{2T} = 0.5$ and $c_{3T} = 0.5$ (solid lines). Using E/ϵ instead of $\overline{TT}/\epsilon_{TT}$ in (27) results in the dashed lines.

	c_{1T}	c'_{1T}	c_{2T}	c'_{2T}	c_{3T}
Dakos & Gibson (1987), Launder (1976)	2.1	0.1	0.96	0.5	0.5
Best results for $Re_\lambda \approx 25$ and $Ri = 1$	1.05	0.05	0.96	0.5	0.5

TABLE 3. Model coefficients of the ϕ_{iT}.

buoyancy-dominated turbulence. Both ϕ_{1T} and $\overline{wT}$ change sign at $t \approx 1.8$ and reach their maximum values at $t \approx 2.7$. The CGHF now diminishes $\overline{uT}$ and the positive ϕ_{1T} balances this sink to keep $\overline{uT}$ at a constant level. Hence, ϕ_{1T} is the direct counterpart of the source term $-S\overline{wT}$ in (15). Component ϕ_{3T} is always negative and of much larger magnitude than ϕ_{1T}. The negative value of ϕ_{3T} keeps $\overline{wT}$ negative as required for a down-gradient flux, see (16). It reaches maximum magnitude at $t \approx 2.0$ when $-\overline{wT}$ experiences the strongest decay rate (figure 3*f*).

As mentioned earlier, ϕ_{iT} is, like ϕ_{ij}, composed of three parts which describe the effects of turbulent–turbulent interactions, shear and buoyancy, see (23*b*). Dakos & Gibson (1987) followed Weinstock's (1986) approach and proposed a model for the turbulent–turbulent and shear contributions. A model for the buoyancy term was derived by Launder (1976). A combination of these models results in

$$\phi_{iT_1} = -c_{1T}\frac{\epsilon_{TT}}{\overline{TT}}\overline{u_i T} + c'_{1T}\,2Eb_{ik}\,s_k, \tag{27}$$

$$\phi_{iT_2} = c_{2T}\,\overline{u_k T}\,S_{ik} + c'_{2T}\,\overline{u_k T}\,S_{ki}, \tag{28}$$

$$\phi_{iT_3} = -c_{3T}\,|Ri_i|\,\overline{TT}, \tag{29}$$

where $s_k = s\delta_{k3}$. The coefficients proposed by Dakos & Gibson (1987) and Launder (1976) are listed in table 3. They are valid for large-Reynolds-number flows which have reached quasi-stationarity. For the reason discussed earlier in this section, the values of c_{1T} and c'_{1T} should be lowered by a factor of about two. Comparison of the

solid curves in figure 15(*b*) with those in figure 15(*a*) shows that for these coefficients the model represents the same qualitative behaviour as found from the direct simulations, at least when the flow has reached a quasi-stationary state.

The closure model requires knowledge of the characteristic timescale of the thermal fluctuations $\overline{TT}/\epsilon_{TT}$ in the turbulence–turbulence term (27). Some closure models solve transport equations for $\overline{TT}$ and ϵ_{TT} (e.g. Elghobashi & Launder 1983) which provide the required timescale. Others usually replace $\overline{TT}/\epsilon_{TT}$ by the velocity timescale E/ϵ. The dashed curves in figure 15(*b*) display the effect of this approximation on the pressure–temperature gradient correlations given by the model. The results show magnitudes for ϕ_{1T} and ϕ_{3T} that are too large, while ϕ_{1T} fails to reflect the sign change that is observed in the direct simulation results.

5.2. *The dissipative timescale ratio*

As explained above, the ratio of the dissipative timescales for kinetic energy and temperature variance

$$r_D \equiv \frac{E/\epsilon}{\overline{TT}/\epsilon_{TT}} \tag{30}$$

is important for models of the pressure–temperature correlations. Furthermore, closure models which do not solve a transport equation for ϵ_{TT} use this ratio to obtain ϵ_{TT} once the values of E, ϵ and $\overline{TT}$ are known. Several experimental and theoretical studies have been performed to investigate the dependency of r_D on other measurable flow quantities to yield an estimate for the thermal dissipation rate. Warhaft & Lumley (1978) measured the decay of the temperature fluctuations in isotropic turbulent flows. They found that the initial value of $\overline{TT}$ determines the development of the turbulent temperature field. Their result for r_D varied between 0.96 and 2.39 and depends on the difference of the peak wavenumber for E and $\overline{TT}$, i.e. on the difference between velocity and temperature lengthscales. After an initial transient development, r_D reaches a constant value. Sirivat & Warhaft (1983) also observed large scatter of r_D around a mean value of 1.3. Their results confirm that r_D depends strongly on the temperature variance of the flow but the authors suggest that the large scatter of r_D may be caused by measuring and calibration errors. By definition, the timescale ratio is proportional to the square of the ratio of microscales of velocity and temperature divided by the Prandtl number. Corrsin (1951) and Budwig *et al.* (1985) determined the ratio of microscales and their result implies that the timescale ratio should be independent of the molecular Prandtl number.

The initial conditions of the present simulations prescribe equal spectra and equal r.m.s. values for velocity and temperature fluctuations, so that the thermal and dynamic lengthscales are also equal. As a consequence, we obtain $r_D = 1/Pr$ initially for all Richardson numbers. Figure 16 illustrates the dependence of the simulation results for r_D on Richardson and Prandtl number. The results show that r_D increases with time and reaches asymptotic values for $4 < t < 6$ depending on Ri and Pr. As stability increases, the timescale ratio stays constant. We have included a case with extreme stability ($Ri = 100$) to illustrate that this constant is enforced when stratification suppresses all vertical motions.

By definition, r_D remains constant if the velocity and temperature fields develop similarly in time. This is certainly the case if the flow behaves linearly so that the length scales for velocity and temperature change at the same rate and thus keep a constant ratio. A linear behaviour is to be expected for strongly stable stratification since then all nonlinear terms are suppressed.

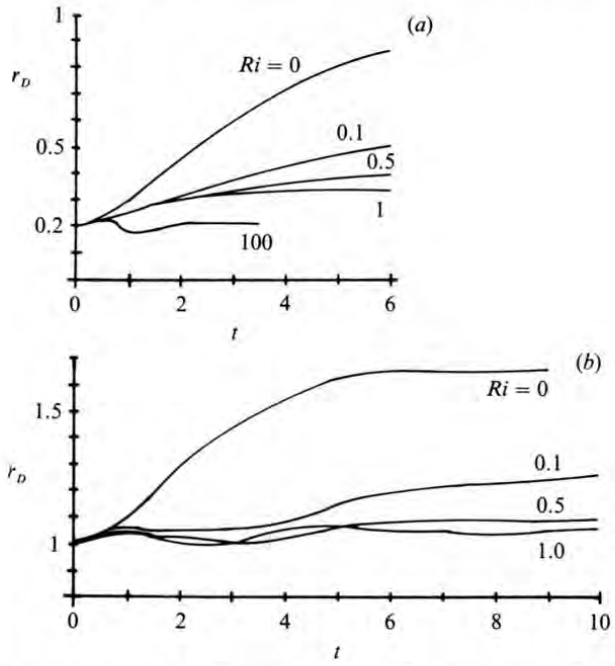

FIGURE 16. Dissipative timescale ratio r_D versus time. (*a*) $Pr = 5$, (*b*) $Pr = 1$ for various Ri values. The results for $Ri = 100$ in (*a*) and for all simulations in (*b*) were obtained from simulations using 32^3 grid points.

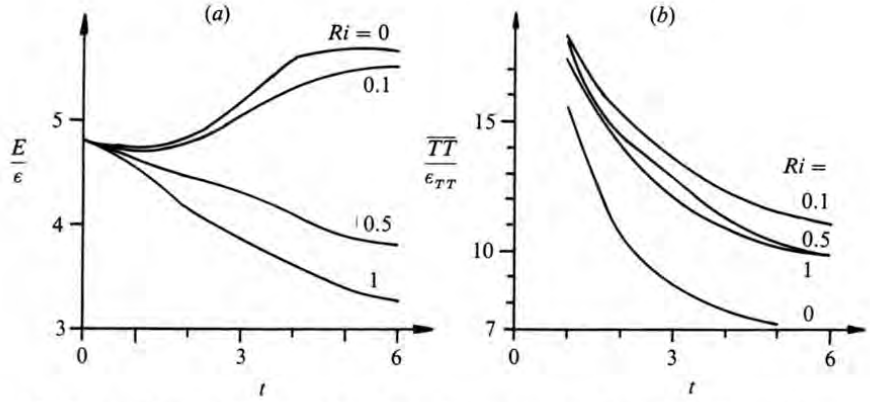

FIGURE 17. Dissipative timescales of (*a*) kinetic energy and (*b*) temperature variance for $Pr = 5$ and several values of the Richardson number.

In a non-stratified shear flow with constant mean temperature, the velocity length- and timescales increase owing to the shear production of turbulence, whereas the timescale of the temperature fluctuations decreases monotonically as can be seen from figure 17. Hence, r_D increases in time as reflected in figure 16 for $Ri = 0$.

If kinetic energy and temperature variance are excited by mean gradients of both temperature and velocity, then r_D achieves values between the limits obtained for zero and very large Richardson numbers. The thermal timescale $\overline{TT}/\epsilon_{TT}$ is rather insensitive to $Ri > 0$, as is indicated by the similarity in the developments of variance and dissipation rate and is corroborated by figure 17 (*b*). On the other hand, the

mechanical timescale E/ϵ depends strongly on Ri (figure 17*a*) because buoyancy affects kinetic energy directly via the term $|Ri|\overline{wT}$ in (14). Initially, shear production dominates and therefore E/ϵ increases while $\overline{TT}/\epsilon_{TT}$ decreases for all Ri. As a consequence, r_D increases with time. This increase, however, is limited by the buoyancy forces so that the maximum value of r_D decreases with increasing Ri. Thus, for large Richardson number the timescale ratio does depend on the molecular Prandtl number whereas for small Richardson number and high Reynolds numbers this dependence diminishes as predicted by Corrsin (1951).

6. Conclusions

We have described a numerical method to investigate homogenous turbulent shear flows with stable stratification. This flow is of importance in many engineering and geophysical applications. The method has been applied to investigate the influence of shear and buoyancy forces on the evolution of homogenous flows for Prandtl numbers of 0.7 (air) and 5 (water) and Richardson numbers between zero and unity.

The Reynolds number is restricted by the number of grid points that we were able to provide on the computer available for this study, particularly so for our cases with rather large Prandtl numbers because $RePr$ controls thermal dissipation. We performed two additional simulations for $Ri = 1$ with 96^3 and 128^3 grid points (details are to be reported elsewhere) which confirm that the present results are not significantly influenced by truncation errors. The Reynolds number, however, is large enough to allow substantial nonlinear interactions as reflected by the time behaviour of velocity-derivative skewness. But it is certainly not large enough to allow direct extrapolation to, say, geophysical applications. In particular, we observed strongly anisotropic dissipation rates which probably are only valid for moderate Reynolds numbers only. On the other hand, the agreement of the simulated flow data with measured data, particularly those from the water-channel experiments of Komori *et al.* (1983) and the wind-tunnel data of Webster (1964), indicates that the essential physical processes and phenomena are described correctly.

The experiments as well as the simulations show that a persistent CGHF occurs in a stably stratified, initially turbulent shear flow if the thermal dissipation rate is too small to limit the ratio of available potential energy to kinetic energy. Large potential energy may originate either from the initial conditions or be produced by velocity fluctuations in stratified flow if the Richardson number Ri is significantly larger than a critical value. This critical value is found to be close to 0.1 for small shear numbers and will approach the linear prediction 0.25 for very large shear numbers. The value of the critical Richardson number in the small-shear-number case depends also on the initial conditions and the Reynolds number.

For strongly stable stratification, regions with large temperature fluctuations develop into hot rising and cold descending dynamically active cells which cause the superposition of small-scale motions on the dominating gravity wave field in the developed flow. These cells degenerate to hot and cold dynamically inert spots (fossil turbulence) if $Pr > 1$ and carry heat counter to the positive gradient of the mean temperature (CGHF). High-Prandtl-number flows are more likely to exhibit the CGHF phenomenon than low-Prandtl-number cases. The same conclusion has also been found from studies using second-order closure models by Schumann (1987). However, it is to be expected that the relative importance of the molecular Prandtl

number diminishes at higher Reynolds numbers. The CGHF can essentially be explained in terms of linear models.

The anisotropy of the normal stresses does not increase monotonically with increasing Ri but achieves a maximum value close to the critical Richardson number and decreases for supercritical Richardson values. The turbulent Prandtl number increases strongly with increasing Ri, achieving infinity when the turbulent vertical heat flux vanishes.

Weinstock (1986) emphasized that the turbulent–turbulent interaction (Rotta term) in the pressure–strain model limits the increase of the anisotropy rather than returning the flow to an isotropic state. The isotropizing effect is still weakened in strongly stable flows while the redistributing contributions from shear and buoyancy become dominant. Optimal values of the model coefficients have been reported for this type of flow at moderate Reynolds numbers.

The pressure–temperature gradient term requires knowledge of the thermal timescale in the turbulence–turbulence term. The reported results corroborate experimental observations which indicate that the dissipative timescale ratio in decaying turbulence always depends on the initial values. The initial value of r_D depends on the molecular Prandtl number. The timescale ratio stays close to this initial value if strong stratification suppresses nonlinear interactions.

The experiments to which we have compared our results in this study have been used by Launder (1975) and others to calibrate second-order closure models. Thus, we are approaching the situation where direct numerical simulations may complement such measurements. We are looking forward to repeating the simulations with the present method for larger Reynolds numbers when the required computer resources become available.

This work was supported by the Deutsche Forschungsgemeinschaft.

REFERENCES

Baron, F. 1982 Macro-simulation tridimensionelle d'ecoulements turbulents cisailles. These de Docteur-Ingenieur, University Pierre et Marie Curie, Paris 6.

Batchelor, G. K. 1953 *The Theory of Homogeneous Turbulence*. Cambridge University Press, pp. 197.

Budwig, R., Tavoularis, S. & Corrsin, S. 1985 Temperature fluctuations and heat flux in grid-generated isotropic turbulence with streamwise and transverse mean-temperature gradients. *J. Fluid Mech.* **153**, 441–460.

Champagne, F. H., Harris, V. G. & Corrsin, S. 1970 Experiments on nearly homogeneous turbulent shear flow. *J. Fluid Mech.* **41**, 81–139.

Corrsin, S. 1951 On the spectrum of isotropic temperature fluctuations in an isotropic turbulence. *J. Appl. Phys.* **22**, 469–473.

Dakos, T. & Gibson, M. M. 1987 On modelling the pressure terms of the scalar flux equations. In *Turbulent Shear Flows 5* (ed. F. Durst *et al.*), pp. 7–18. Springer.

Deardorff, J. W. 1966 The counter-gradient heat flux in the lower atmosphere and in the laboratory. *J. Atmos. Sci.* **23**, 503–506.

Elghobashi, S. E. & Launder, B. E. 1983 Turbulent time scales and the dissipation rate of temperature variance in the thermal mixing layer. *Phys. Fluids* **26**, 2415–2419.

Gerz, T. 1988*a* Direkte Simulation stabil geschichteter, homogen-turbulenter Scherströmungen. Dissertation Ludwig-Maximilians-Universität Munich, *Deutsche Forschungs- und Versuchsanstalt für Luft- und Raumfahrt, Cologne, Rep.* DFVLR-FB 88-04.

GERZ, T. 1988*b* Direct simulation of stably stratified homogeneous turbulent shear flows. In *Proc. 8th Symp. on Turbulence and Diffusion, April 25–29, 1988, San Diego*, pp. 66–69.

GIBSON, C. H. 1987 Fossil turbulence and intermittency in sampling oceanic mixing processes. *J. Geophys. Res.* **92**, C5, 5383–5404.

GILL, A. E. 1982 *Atmosphere–Ocean Dynamics*. Academic.

HARRIS, V. G., GRAHAM, J. A. H. & CORRSIN, S. 1977 Further experiments in nearly homogeneous turbulent shear flow. *J. Fluid Mech.* **81**, 657–687.

HUNT, J. C. R., STRETCH, D. D. & BRITTER, R. E. 1988 Length scales in stably stratified turbulent flows and their use in turbulence models. In *Stably Stratified Flow and Dense Gas Dispersion* (ed. J. S. Puttock), pp. 285–321. Clarendon.

ITSWEIRE, E. C., HELLAND, K. N. & VAN ATTA, C. W. 1986 The evolution of grid-generated turbulence in a stably stratified fluid. *J. Fluid Mech.* **162**, 299–338.

KOMORI, S., UEDA, H., OGINO, F. & MIZUSHINA, T. 1983 Turbulence structure in stably stratified open-channel flow. *J. Fluid Mech.* **130**, 13–26.

LAUNDER, B. E. 1975 On the effects of a gravitational field on the turbulent transport of heat and momentum. *J. Fluid Mech.* **67**, 569–581.

LAUNDER, B. E. 1976 Heat and mass transport. In *Turbulence* (ed. P. Bradhaw), Topics in Applied Physics, vol. 12, pp. 232–287. Springer.

LAURENCE, D. 1986 Advective formulation of large eddy simulations for engineering type flows. In *Direct and Large Eddy Simulations* (ed. U. Schumann & R. Friedrich), Notes on Numerical Fluid Mechanics, vol. 15, pp. 147–160. Vieweg.

MILES, J. W. 1961 On the stability of heterogeneous shear flows. *J. Fluid Mech.* **10**, 496–508.

RILEY, J. J., METCALFE, R. W. & WEISSMAN, M. A. 1981 Direct numerical simulations of homogeneous turbulence in density-stratified fluids. In *Nonlinear Properties of Internal Waves* (ed. B. J. West), AIP Conf., vol. 76, pp. 79–112.

ROGALLO, R. S. 1981 Numerical experiments in homogeneous turbulence. *NASA TM* 81315.

ROGALLO, R. S. & MOIN, P. 1984 Numerical simulation of turbulent flows. *Ann. Rev. Fluid Mech.* **16**, 99–137.

ROGERS, M. M. & MOIN, P. 1987 The structure of the vorticity field in homogeneous turbulent flows. *J. Fluid Mech.* **176**, 33–66.

ROGERS, M. M., MOIN, P. & REYNOLDS, W. C. 1986 The structure and modeling of the hydrodynamic and passive scalar fields in homogeneous turbulent shear flow. *Dept. Mech. Eng., Stanford University, California, Tech. Rep.* TF-25.

ROHR, J. J., ITSWEIRE, E. C., HELLAND, K. N. & VAN ATTA, C. W. 1988 An investigation of the growth of turbulence in a uniform-mean-shear flow. *J. Fluid Mech.* **187**, 1–33.

SCHUMANN, U. 1985 Algorithms for direct numerical simulation of shear-periodic turbulence. In *Proc. 9th Intl Conf. on Numerical Meth. in Fluid Dyn.* (ed. Soubbaramayer & J. P. Boujot). Lecture Notes in Physics, vol. 218, pp. 492–496. Springer.

SCHUMANN, U. 1987 The countergradient heat flux in turbulent stratified flows. *Nucl. Engrg Des.* **100**, 255–262.

SCHUMANN, U., ELGHOBASHI, S. & GERZ, T. 1986 Direct simulation of stably stratified turbulent homogeneous shear flows. In *Direct and Large Eddy Simulations* (ed. U. Schumann & R. Friedrich), Notes on Numerical Fluid Mechanics, vol. 15, pp. 245–264. Vieweg.

SHIRANI, E., FERZIGER, J. H. & REYNOLDS, W. C. 1981 Mixing of a passive scalar in isotropic and sheared homogeneous turbulence. *Thermosciences Div., Dept. Mech. Eng., Stanford University, California, Tech. Rep.* TF-15.

SIRIVAT, A. & WARHAFT, Z. 1983 The effect of a passive cross-stream temperature gradient on the evolution of temperature variance and heat flux in grid turbulence. *J. Fluid Mech.* **128**, 323–346.

STEWART, R. W. 1969 Turbulence and waves in a stratified atmosphere. *Radio Sci.* **4**, 1269–1278.

STILLINGER, D. C., HELLAND, K. N. & VAN ATTA, C. W. 1983 Experiments on the transition of homogeneous turbulence to internal waves in a stratified fluid. *J. Fluid Mech.* **131**, 91–122.

TAVOULARIS, S. & CORRSIN, S. 1981 Experiments in nearly homogeneous turbulent shear flow with a uniform mean temperature gradient. Part 1. *J. Fluid Mech.* **104**, 311–347.

WARHAFT, Z. & LUMLEY, J. L. 1978 An experimental study of the decay of temperature fluctuations in grid-generated turbulence. *J. Fluid Mech.* **88**, 659–684.

WEBSTER, C. A. G. 1964 An experimental study of turbulence in a density stratified shear flow. *J. Fluid Mech.* **19**, 221–245.

WEINSTOCK, J. 1986 Theoretical pressure–strain term in a stratified fluid. *J. Fluid Mech.* **172**, 17–31.

ZEMAN, O. & LUMLEY, J. L. 1976 Modeling buoyancy driven mixed layers. *J. Atmos. Sci.* **33**, 1974–1988.